AGU PUBLICATIONS

JGR

Journal of Geophysical Research: Space Physics

RESEARCH ARTICLE

10.1002/2016JA023828

Key Points:

- TIDs used to determine neutral wind and density perturbations from gravity waves
- Serious discrepancy between gravity wave theory and observation can be resolved by a decreasing molecular viscosity mu in the thermosphere
- Mu decreasing in thermosphere allows gravity waves to propagate much higher than previously thought

Correspondence to:
S. L. Vadas,
vasha@cora.nwra.com

Citation:
Vadas, S. L. and G. Crowley (2017), Neutral wind and density perturbations in the thermosphere created by gravity waves observed by the TIDDBIT sounder, *J. Geophys. Res. Space Physics*, *122*, 6652–6678, doi:10.1002/2016JA023828.

Received 20 DEC 2016
Accepted 7 MAY 2017
Accepted article online 12 MAY 2017
Published online 10 JUN 2017

Neutral wind and density perturbations in the thermosphere created by gravity waves observed by the TIDDBIT sounder

Sharon L. Vadas[1] and Geoff Crowley[2]

[1]Northwest Research Associates/CoRA Office, Boulder, Colorado, USA, [2]Atmospheric and Space Technology Research Associates, Boulder, Colorado, USA

Abstract In this paper, we study the 10 traveling ionospheric disturbances (TIDs) observed at $z_{\rm obs} \sim 283$ km by the TIDDBIT ionospheric sounder on 30 October 2007 at 0400–0700 UT near Wallops Island, USA. These TIDs propagated northwest/northward and were previously found to be secondary gravity waves (GWs) from tropical storm Noel. An instrumented sounding rocket simultaneously measured a large neutral wind peak u'_H with a similar azimuth at $z \sim 325$ km. Using the measured TID amplitudes and wave vectors from the TIDDBIT system, together with ion-neutral theory, GW dissipative polarization relations and ray tracing, we determine the GW neutral horizontal wind and density perturbations as a function of altitude from 220 to 380 km. We find that there is a serious discrepancy between the GW dissipative theory and the observations unless the molecular viscosity, μ, decreases with altitude in the middle to upper thermosphere. Assuming that $\mu \propto \bar{\rho}^q$, where $\bar{\rho}$ is the density, we find using GW dissipative theory that the GWs could have been observed at $z_{\rm obs}$ and that one or more of the GWs could have caused the u'_H wind peak at $z \simeq 325$ km if $q \sim 0.67$ for $z \geq 220$ km. This implies that the kinematic viscosity, $\nu = \mu/\bar{\rho}$, increases less rapidly with altitude for $z \geq 220$ km: $\nu \propto 1/\bar{\rho}^{0.33}$. This dependence makes sense because as $\bar{\rho} \to 0$, the distance between molecules goes to infinity, which implies no molecular collisions and therefore no molecular viscosity μ.

1. Introduction

The TIDDBIT system is a Doppler radar system which measures the propagation properties of traveling ionospheric disturbances (TIDs) such as horizontal wavelength, azimuth, period, and horizontal phase speed. This system was installed at Wallops Island, Virginia (75.47°W and 37.95°N), for approximately 5 weeks during the fall of 2007 and consisted of three transmitters and one receiver [*Crowley and Rodrigues*, 2012]. During this time, an instrumented sounding rocket was launched into a midlatitude spread *F* condition at 0412 UT (12:12 A.M. local time) on 30 October. Among other quantities, the instruments on this rocket measured the direction and amplitude of the neutral wind. From 0400 to 0700 UT on 30 October (during the launch window), 10 TIDs were observed by TIDDBIT at the altitude $z_{\rm obs} \simeq 283$ km. These waves were all propagating northwest or northward. Via comparison with atmospheric gravity wave (GW) dissipative theory, *Vadas and Crowley* [2010, hereafter VC10] showed that these TIDs were likely created by GWs. VC10 also showed that it was likely that these GWs were so-called "secondary" GWs from tropical storm (TS) Noel. In this two-step coupling process, primary GWs created by TS Noel propagated into the thermosphere where they dissipated from molecular viscosity and thermal conduction. This dissipation accelerated the background fluid in the horizontal direction of GW propagation, creating so-called "thermospheric body forces." Such body forces excite secondary GWs [*Vadas and Liu*, 2009, 2013].

The instrumented sounding rocket measured the neutral horizontal wind from $z \sim 320$ to 385 km; this wind was found to be northwestward (opposite to the expected direction of the wind from the tides at this time) and was found to vary significantly in amplitude over this altitude range [*Earle et al.*, 2010]. This vertical variation was surprising, because viscosity was thought to smooth out vertical variations in the wind at this altitude. Figure 8 from that paper is reproduced here as Figure 1. Figure 1b shows the azimuth, θ, of the horizontal component of the neutral wind (clockwise from north). We see that θ decreased from $\theta \simeq -45°$ to $-60°$ (i.e., from 315° to 300°) over this altitude range. Figure 1a shows the horizontal neutral wind amplitude.

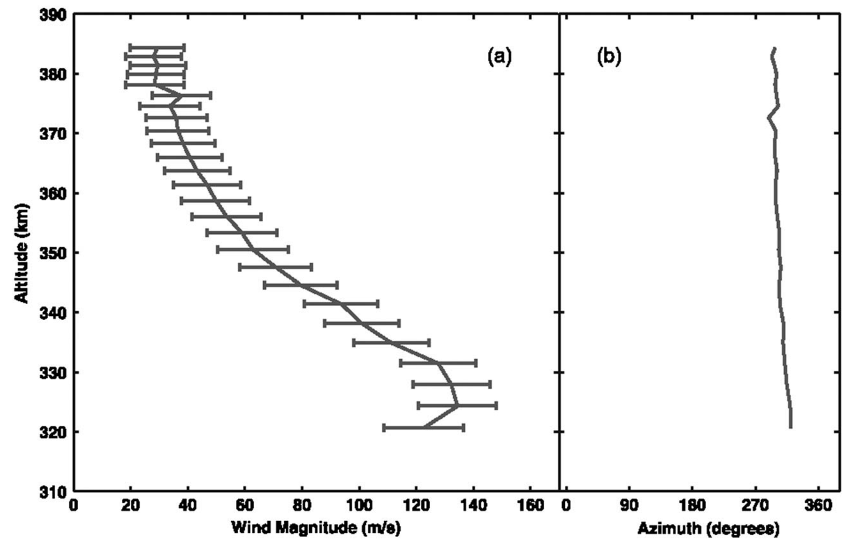

Figure 1. *F* region horizontal neutral wind (a) magnitude and (b) direction in the Earth-fixed reference frame measured by the sounding rocket. This was calculated under the assumption that the vertical wind component was negligible compared to the horizontal wind component. This is Figure 8 reproduced from *Earle et al.* [2010].

It peaked at $z \sim 325$ km with a value of $\sim(130 \pm 20)$ m/s and decreased rapidly to $\sim(30 \pm 10)$ m/s at $z \sim 385$ km. This figure was created assuming that the vertical wind component was negligible compared to the horizontal wind component.

It is thought that (1) the largest-amplitude tidal component at $z \geq 200$ km is the migrating diurnal tide and (2) the amplitude and azimuth of the horizontal wind from this tide do not change appreciably for $z > 200$ km because of molecular viscosity [*Roble and Ridley*, 1994] and ion drag [*Becker*, 2017]. Therefore, the neutral wind maximum at $z \sim 325$ km and its subsequent significant decrease at higher altitudes in Figure 1a was unlikely due to this or to any other tide. Additionally, the climatology horizontal wind component from the tides was estimated using the thermosphere-ionosphere-mesosphere-electrodynamics general circulation model (TIME-GCM) [*Roble and Ridley*, 1994; *Crowley et al.*, 2008] to be southeastward at that time and location, with an amplitude of ∼40 m/s (VC10). Therefore, the wind measured by the sounding rocket might have been the sum of a southeastward tidal wind component plus a large northwestward wind component having an altitudinally varying amplitude of ∼170 to ∼70 m/s from $z = 325$ km to 385 km, respectively.

There are several reasons to postulate that this large northwestward wind component might have been created by one or more of the GWs measured by the TIDDBIT sounder:

1. All 10 TIDDBIT GWs were propagating northwestward or northward, and those with the largest horizontal wavelengths λ_H and largest horizontal phase speeds c_H (expected to reach the highest altitudes prior to dissipating [*Vadas*, 2007]) were propagating in approximately the same direction as the measured wind (northwestward). Furthermore, all 10 GWs were "high frequency" because they had frequencies much larger than the Coriolis frequency. Since a high-frequency GW has its horizontal wind perturbation parallel and antiparallel to its propagation direction [e.g., *Fritts and Alexander*, 2003; *Vadas and Fritts*, 2005], these TIDDBIT GWs would therefore have induced northwestward and southeastward wind perturbations in the thermosphere. Therefore, it is conceivable that the large northwestward wind component measured by the sounding rocket was due to one or more of the TIDDBIT GWs.
2. Assuming that one of the TIDDBIT GWs had a maximum horizontal wind amplitude, u'_H, at $z \sim 325$ km, the rapid decay of the wind with altitude for $z > 325$ km is consistent with GW dissipative theory [*Vadas*, 2007]. In particular, if z_{diss} is the altitude where the GW momentum flux per unit mass, $\overline{u'_H w'}$, is maximum, then $\overline{u'_H w'}$ decreases rapidly with altitude for $z > z_{\text{diss}}$ up to $z \sim z_{\text{diss}} + \text{H}$, where H is the neutral density scale height; above this altitude, $\overline{u'_H w'}$ is insignificant. The TIME-GCM suggests that $H \sim 30-35$ km that evening at $z \sim 300-350$ km.

For the above reasons, *Earle et al.* [2010] suggested that some of the TIDDBIT GWs might have created the observed large and altitudinally varying northwestward wind at $z \sim 320-385$ km. However, no detailed study was made in that paper to prove or disprove this hypothesis.

The purpose of this paper is to investigate this hypothesis in detail. We review the GW dissipative dispersion and polarization relations used in ray tracing and for calculating the GW perturbations as a function of altitude in section 2. In section 3, we describe the properties of the TIDDBIT TIDs. We review the equations expressing the ion perturbations created by a GW using the single ion approximation in section 4. We also derive the equations used to determine a GW's momentum flux amplitude at the observation altitude from the vertical ion displacement of the TID. In section 5, we forward ray trace the GWs through various background atmospheres in order to determine the GW momentum flux, horizontal velocity, and density perturbations as a function of altitude. We include all major species in the expressions for the molecular viscosity and thermal conductivity in section 6. Our conclusions are provided in section 7.

2. GW Dissipative Relations and Altitudinally Varying GW Perturbations

In this section, we review the GW dissipative dispersion and polarization relations, the amplitude decay rate in time, and the procedure by which we determine the GW perturbations as a function of altitude via ray tracing.

2.1. GW Dissipative Dispersion Relation and Amplitude Decay in Time

The thermosphere begins at the turbopause ($z \sim 107$ km) and extends up to $z \sim 500-600$ km. It is characterized by a rapidly increasing kinematic viscosity with altitude, $\nu = \mu/\bar{\rho}$, where μ is the molecular viscosity and $\bar{\rho}$ is the background neutral density [*Hines*, 1960]. Molecular viscosity results from collisions between neutral molecules. As the thermosphere becomes more rarefied with increasing altitude, molecular collisions are less frequent, so that the velocity amplitude and direction of the molecules associated with a GW are not transmitted effectively, thereby damping the GW [*Pitteway and Hines*, 1963; *Hickey and Cole*, 1988; *Vadas*, 2007; *Yiğit et al.*, 2009; *Walterscheid and Hickey*, 2011; *Heale et al.*, 2014].

The GW dispersion relation we use here for ray tracing is [*Vadas and Fritts*, 2005, hereafter VF05; *Vadas and Nicolls*, 2009]:

$$m^2 = \frac{k_H^2 {N_B}^2}{\omega_{Ir}^2\left(1+\delta_+ + \delta^2/Pr\right)}\left[1+\frac{\nu^2}{4\omega_{Ir}^2}\left(\mathbf{k}^2 - \frac{1}{4H^2}\right)^2 \frac{(1-Pr^{-1})^2}{(1+\delta_+/2)^2}\right]^{-1} - k_H^2 - \frac{1}{4H^2}, \quad (1)$$

where ω_{Ir} is the real part of the complex intrinsic frequency; k, l, and m are the zonal, meridional, and vertical wave numbers, respectively; $k_H = \sqrt{k^2+l^2}$ is the horizontal wave number; $\mathbf{k}^2 = k_H^2 + m^2$; N_B is the buoyancy frequency; $H = -\bar{\rho}(d\bar{\rho}/\mathrm{d}z)^{-1}$ is the neutral density scale height; $\bar{\rho}$ is the background neutral density; $\nu = \mu/\bar{\rho}$ is the kinematic viscosity; μ is the molecular viscosity; $\kappa = \nu/Pr$ is the thermal diffusivity; Pr is the Prandtl number; $\delta = \nu m/\mathrm{H}\omega_{Ir}$; and $\delta_+ = \delta(1+Pr^{-1})$. The zonal, meridional, and vertical wavelengths are $\lambda_x = 2\pi/k$, $\lambda_y = 2\pi/l$, and $\lambda_z = 2\pi/m$, respectively, and the horizontal wavelength is $\lambda_H = 2\pi/k_H$. For an upward propagating GW, δ is negative because $m < 0$. This dispersion relation is anelastic and includes molecular viscosity and thermal conduction, the main mechanisms for damping high-frequency GWs in the thermosphere. It neglects ion drag, which is appropriate for GWs having periods less than one to several hours [e.g., *Gossard and Hooke*, 1975] and neglects wave-induced diffusion, which is appropriate for GWs having periods less than an hour [*DelGenio and Schubert*, 1979]. It also neglects the Coriolis force, which is appropriate for GWs having periods less than a few hours.

A GW's intrinsic frequency is related to its observed frequency, $\omega_r = 2\pi/\tau_r$, via

$$\omega_r = \omega_{Ir} + kU + lV = \omega_{Ir} + k_H U_H, \quad (2)$$

where U and V are the background zonal and meridional winds, respectively,

$$U_H = (k\,U + l\,V)/k_H \quad (3)$$

is the projection of the background neutral wind along the propagation direction of the GW, and τ_r is the observed GW period. When dissipation is negligible (i.e., $\nu = \delta = 0$), equation (1) reduces to the familiar GW anelastic dispersion relation:

$$\omega_{Ir}^2 \simeq \frac{k_H^2 {N_B}^2}{m^2 + k_H^2 + \frac{1}{4H^2}} \quad (4)$$

[*Gossard and Hooke*, 1975; *Marks and Eckermann*, 1995]. Because we consider the dissipation of a GW packet explicitly in time and implicitly in z (rather than explicitly in z and independent of time, which results in a steady state GW solution), we assume a complex intrinsic frequency ω_I (rather than a complex vertical wave number m). Thus, the ansatz utilized to derive equation (1) is as follows:

$$\omega_I = \omega_{Ir} + i\omega_{Ii}, \tag{5}$$

where ω_{Ii} is the inverse decay rate in time of a GW. Because a GW's amplitude is proportional to $\exp(-i\omega_I t) = \exp(\omega_{Ii} t)\exp(-i\omega_{Ir} t)$, a GW decays explicitly in time here rather than explicitly in altitude. This ansatz results in an inverse decay rate in time of

$$\omega_{Ii} = -\frac{\nu}{2}\left(\mathbf{k}^2 - \frac{1}{4H^2}\right)\frac{[1+(1+2\delta)/Pr]}{(1+\delta_+/2)} \tag{6}$$

(VF05). Note that ω_{Ii} varies significantly along a GW's raypath.

Equation (1) was derived using the WKB approximation, and therefore is appropriate for use in ray tracing when the parameters vary slowly enough [*Godin*, 2015]. The residue, R, can be used to indicate when ray tracing is valid [*Einaudi and Hines*, 1970; VF05]:

$$R = \frac{1}{2m^3}\frac{\mathrm{d}^2 m}{\mathrm{d}z^2} - \frac{3}{4m^4}\left(\frac{\mathrm{d}m}{\mathrm{d}z}\right)^2; \tag{7}$$

if $R > 1$, the WKB approximation can fail because the solution cannot be written as a single upgoing or downgoing GW, since strong dissipation causes an upward propagating GW to partially reflect downward [*Yanowitch*, 1967; *Ma*, 2016]. If we define z_{diss} to be the altitude where a GW's momentum flux, $\overline{u'_H w'}$, is maximum, then $R \simeq 1$ typically occurs at $z \sim z_{\mathrm{diss}} + H$. At this altitude, the GW's momentum flux is typically $\overline{u'_H w'} < \overline{u'_H w'}(z_{\mathrm{diss}})/2$ [*Vadas*, 2007]. This occurs well below the altitude, z_{refl}, where a GW appears to reflect downward due to viscosity if the $R \le 1$ criteria is ignored (VF05). However, these criteria should not be ignored because upward and downward propagating GWs are created in the presence of strong dissipation (i.e., where $z \sim z_{\mathrm{refl}}$) [*Yanowitch*, 1967; *Ma*, 2016], which nullifies the necessary condition for ray tracing (i.e., that only a single upward or downward propagating GW exists). Therefore, ray tracing should not be performed up to $z \sim z_{\mathrm{refl}}$ (as was mistakenly done in VF05), because dissipation is too strong there. However, because $\overline{u'_H w'}$ is quite small at and above the altitude where $R \simeq 1$ [*Vadas*, 2007], we expect that past results for spectra of GWs which did not eliminate GWs with $R \ge 1$ would not be substantially different than if those GWs had been eliminated instead [e.g., *Vadas and Liu*, 2013]. As a support of this statement, a recent numerical study integrated the 2-D Navier Stokes fluid equations in the thermosphere and found that the results for the viscous dissipation of a linear GW are quite similar to that of the WKB VF05 ray trace results [*Liu et al.*, 2013].

2.2. GW Dissipative Polarization Relations

As a linear GW dissipates in the thermosphere, the amplitudes and phases between the various perturbation components (such as velocity, temperature, and density) change [VF05; *Vadas and Nicolls*, 2012]. The equations which describe these changes are called the GW polarization relations. These expressions differ from the usual GW dispersion relations [e.g., *Fritts and Alexander*, 2003; *Vadas*, 2013] in that they include GW dissipation from kinematic viscosity and thermal diffusivity.

We set the background temperature $T = \bar{T}$ to be constant (i.e., isothermal) for the purpose of deriving the GW polarization relations. (Afterward, these relations can be applied to a fluid with a slowly varying background.) This results in a background neutral density which varies exponentially with altitude: $\bar{\rho} = \bar{\rho}_0 \exp(-z/H)$, where $\bar{\rho}_0$ is the background density at $z = 0$ and overlines denote mean values [*Hines*, 1960]. We define density-scaled perturbations as

$$\begin{aligned} &\tilde{u} = \mathrm{e}^{-z/2\mathrm{H}} u', \qquad \tilde{v} = \mathrm{e}^{-z/2\mathrm{H}} v', \qquad \tilde{w} = \mathrm{e}^{-z/2\mathrm{H}} w', \qquad \widetilde{u_H} = \mathrm{e}^{-z/2\mathrm{H}} u'_H, \\ &\tilde{\rho} = \mathrm{e}^{z/2\mathrm{H}} \rho', \qquad \tilde{T} = \mathrm{e}^{-z/2\mathrm{H}} T', \end{aligned} \tag{8}$$

where primes denote perturbations, tildes "$\sim$" denote the density-scaled variables, $u'_H = \sqrt{(u')^2 + (v')^2}$ is the GW horizontal velocity perturbation (positive by definition), and

$$u' = \frac{k}{k_H} u'_H, \qquad v' = \frac{l}{k_H} u'_H. \tag{9}$$

Here the GW perturbation variables are the zonal, meridional, and vertical velocities u', v', and w', respectively, the density ρ', and the temperature T'. We linearize the fluid equations. We then write each perturbation component in equation (8) as, for example,

$$\tilde{u} = \tilde{u}_0 \exp[i(kx + ly + mz - \omega t)], \tag{10}$$

where ω is the complex frequency and ω_I is the intrinsic frequency:

$$\omega_I = \omega - kU - lV, \tag{11}$$

and $\tilde{u}_0$, $\tilde{v}_0$, etc. are the amplitudes of the GW at (x, y, z, t). The dissipative anelastic GW polarization relations interrelating these perturbations are [VF05; *Vadas and Nicolls*, 2009, 2012]:

$$\frac{\tilde{w}_0}{\widetilde{u_{H0}}} = -\frac{k_H m}{m^2 + \frac{1}{4H^2}} \left[1 - \frac{i\left(\mathbf{k}^2 + \frac{1}{4H^2}\right)(\omega_I - i\alpha\nu)}{2mHk_H^2 N_B{}^2} \left[\left(\frac{2}{\gamma} - 1\right)\omega_I - \frac{i\alpha\nu}{Pr} \right] \right], \tag{12}$$

$$\frac{\tilde{T}_0}{\tilde{w}_0} \simeq \frac{(\gamma - 1)\bar{T}}{H\mathcal{D}} \left(im + \frac{1}{2H} \right), \tag{13}$$

$$\frac{\tilde{\rho}_0}{\tilde{w}_0} \simeq -\frac{(\gamma - 1)\bar{\rho}_0}{H\mathcal{D}} \left(im - \frac{1}{2H} \right), \tag{14}$$

$$\frac{\tilde{u}_0}{\widetilde{u_{H0}}} = \frac{k}{k_H}, \tag{15}$$

$$\frac{\tilde{v}_0}{\widetilde{u_{H0}}} = \frac{l}{k_H}, \tag{16}$$

where

$$\alpha \equiv -\mathbf{k}^2 + \frac{1}{4H^2} + \frac{im}{H}, \tag{17}$$

$$\mathcal{D} = \left[i\omega_I \left(\gamma im + \frac{1}{H} - \frac{\gamma}{2H} \right) + \frac{\gamma\alpha\nu}{Pr} \left(im + \frac{1}{2H} \right) \right], \tag{18}$$

$\gamma - 1 = \mathrm{R}/C_v$, and C_v is the mean specific heat at constant volume, $R = (8314/X_{\mathrm{MW}})\,\mathrm{m^2\,s^{-2}\,K^{-1}}$, and X_{MW} is the mean molecular weight of a molecule in the fluid (in g/mol). Note that the right-hand sides of equations (12)–(16) only depend on the parameters of a GW (such as (k, l, m) and ω_{Ir}) and on the background parameters (such as H and N_B), and not on the GW amplitude. In general, the ratios $\tilde{w}_0/\widetilde{u_{H0}}$, $\tilde{T}_0/\tilde{w}_0$, $\tilde{\rho}_0/\tilde{w}_0$, $\tilde{u}_0/\widetilde{u_{H0}}$, and $\tilde{v}_0/\widetilde{u_{H0}}$ are complex and thus can be written as $a\exp(ib)$, where a is the ratio of the amplitudes and b is the phase difference between the components. Equations (8) and (10) are then used to extract the perturbation amplitude and phases. For example, using equations (8), (10), and (14), the ratio of the density perturbation to the vertical velocity perturbation is

$$\frac{\rho'}{w'} = \left(\frac{\bar{\rho}}{\bar{\rho}_0}\right)\left(\frac{\tilde{\rho}_0}{\tilde{w}_0}\right) = -\frac{(\gamma - 1)\bar{\rho}}{\mathrm{H}\mathcal{D}} \left(im - \frac{1}{2H} \right). \tag{19}$$

2.3. Altitudinally Varying GW Momentum Flux, Velocity, and Density Perturbations

We now show how the perturbation quantities of a GW are determined along its raypath via ray tracing. The initial momentum flux of a GW at $\mathbf{x} = \mathbf{x}_i$ and $t = t_i$ is $\overline{u'_H w'}(\mathbf{x}_i, t_i)$. The momentum flux of this GW at a later time t and location $\mathbf{x}$ along its raypath is [*Vadas and Fritts*, 2009] as follows:

$$\overline{u'_H w'}(\mathbf{x}, t) = \overline{u'_H w'}(\mathbf{x}_i, t_i)\frac{\bar{\rho}(z_i)}{\bar{\rho}(z)} \exp\left(-2\int_{t_i}^{t} |\omega_{Ii}| \mathrm{d}t' \right), \tag{20}$$

where we put an absolute value around ω_{Ii} to ensure that the GW dissipates even if $\mathbf{k}^2 < 1/4H^2$ and where the integral of $|\omega_{Ii}|$ is performed along the raypath. The horizontal and vertical velocity, temperature, and density perturbations along the raypath are then

$$w' = \sqrt{\left|\frac{\tilde{w}_0}{\widetilde{u_{H0}}}\right| \overline{u'_H w'}}, \tag{21}$$

$$u'_H = \left(\frac{\tilde{w}_0}{\widetilde{u_{H0}}}\right)^{-1} w', \tag{22}$$

$$u' = \left(\frac{\tilde{u}_0}{\widetilde{u_{H0}}}\right) u'_H, \tag{23}$$

$$v' = \left(\frac{\tilde{v}_0}{\widetilde{u_{H0}}}\right) u'_H, \tag{24}$$

$$T' = \left(\frac{\tilde{T}_0}{\tilde{w}_0}\right) w', \tag{25}$$

$$\rho' = \frac{\bar{\rho}}{\bar{\rho}_0} \left(\frac{\tilde{\rho}_0}{\tilde{w}_0}\right) w', \tag{26}$$

where the phases are defined relative to the phase of w', and equation (26) is obtained from equation (19). Here, $(\tilde{u}_0/\widetilde{u_{H0}})$, $(\tilde{v}_0/\widetilde{u_{H0}})$, $(\tilde{w}_0/\widetilde{u_{H0}})$, $(\tilde{T}_0/\tilde{w}_0)$ and $(\tilde{\rho}_0/\tilde{w}_0)$ are calculated from equations (12)–(16), and

$$\left|\frac{\tilde{w}_0}{\widetilde{u_{H0}}}\right| = \sqrt{\left(\frac{\tilde{w}_0}{\widetilde{u_{H0}}}\right)\left(\frac{\tilde{w}_0}{\widetilde{u_{H0}}}\right)^*}, \tag{27}$$

where the "asterisk" denotes the complex conjugate. In general u', v', u'_H, T' and ρ' are complex numbers and thereby have nonzero phases relative to w' in general. Note that equations (21)–(26) do not take into account the decrease of a GW's amplitude due to the geometric spreading of a wave packet in time, which is proportional to $1/z^2$. This is likely adequate here, because the TIDDBIT GWs are medium to large scale, and their momentum fluxes are only computed from $z_i = 220$ km to $z \sim 385$ km.

3. Properties of the TIDDBIT TIDs During the Rocket Launch Window

Table 1 sums up the properties of the 10 TIDs observed from 0400 to 0700 UT by the TIDDBIT sounder. The height of these measurements was estimated from a local ionosonde to be $z \sim 283$ km (VC10). This time window was chosen to overlap with sounding rocket measurements [*Earle et al.*, 2010]. These TIDDBIT data have been reanalyzed using slightly different criteria than were used in VC10. Although there are differences in the TID properties between this analysis and VC10, they are relatively small and are within the error bars. (Note that because VC10 analyzed the data every 30 min, the same GWs were seen in nearly all of the six 30 min time bins within this 3 h period. Here, however, we utilize a somewhat different analysis method to determine all of the GWs within the entire 3 h bin. This is why we only identify 10 TIDs here, whereas we identified 59 TIDs over the six 30 min time bins in VC10 (see section 4.2 in VC10).) The columns, from left to right, show the measured wave period τ_r, horizontal phase speed c_H, azimuth θ (clockwise from north), horizontal wavelength λ_H, Doppler wave amplitude A_i (in Hz), and Doppler wave amplitude h_i (in km). Uncertainty estimates are included for all quantities. Note that some of the errors are larger than the measured values. These error bars are obtained in a similar way as done previously [e.g., VC10; *Crowley and Rodrigues*, 2012] and provide an overestimate of the actual error. A newly developed method using a least squares analysis method results in much smaller error bars on the wave speed and azimuth. This new method will be discussed in a future publication. In Table 1, all 10 TIDs propagated northward or northwestward. Here A_i comes

Table 1. Parameters of TIDDBIT Waves Observed on 30 October 2007 From 0400 to 0700 UT

Wave #	τ_r (min)	c_H (m/s)	θ (deg)	λ_H (km)	A_i (Hz)	h_i (km)
1	16.3	177 ± 28	-30 ± 10	174 ± 28	$0.023 \pm .001$	$0.158 \pm .008$
2	16.3	259 ± 18	-27 ± 11	254 ± 18	0.019 ± 0.0085	0.143 ± 0.057
3	18.0	164 ± 6	-16 ± 3	177 ± 7	0.032 ± 0.006	0.246 ± 0.045
4	18.0	229 ± 12	-15 ± 4	248 ± 13	0.031 ± 0.013	0.255 ± 0.105
5	20.0	155 ± 22	-6 ± 11	186 ± 27	0.027 ± 0.003	0.225 ± 0.029
6	20.0	160 ± 37	3 ± 9	192 ± 45	0.018 ± 0.007	0.161 ± 0.063
7	36.0	263 ± 427	-48 ± 63	568 ± 924	0.052 ± 0.024	0.852 ± 0.399
8	45.0	398 ± 356	-24 ± 36	1077 ± 962	0.059 ± 0.013	1.113 ± 0.256
9	45.0	592 ± 3400	-56 ± 12	1599 ± 9189	0.043 ± 0.013	0.872 ± 0.271
10	60.0	497 ± 328	-18 ± 10	1789 ± 1183	0.068 ± 0.011	1.716 ± 0.286

from the Fourier transform of the Doppler shifts on each transmission path and is an average value from the three transmitters. We define the height of the wave amplitude at the radio reflection height to be h_i. This amplitude is related to the Doppler wave amplitude, A_i, via

$$h_i = \frac{A_i c_s \tau_r}{4\pi F_{\text{transmit}}}. \tag{28}$$

Here A_i is in hertz, h_i is in meters, c_s is the speed of light in m/s, τ_r is the wave period in seconds, and F_{transmit} is the broadcast frequency of the TIDDBIT system in hertz (e.g., 3.397×10^6 Hz). Equation (28) combines the standard equation which converts the Doppler shift to the velocity (i.e., velocity$= A_i c_s/F_{\text{transmit}}$) and integrates to get the wave amplitude (i.e., multiplies by $\tau_r/2\pi$). We divide by 2 in the denominator of equation (28) because the Doppler technique involves reflection from the ionosphere, which doubles the path length. Note that the height of the wave amplitude, h_i, is the absolute value of the displacement that the ions make over 1/4 of a wave cycle (i.e., from 0 to $\pi/2$ in phase).

4. Traveling Ionospheric Disturbance Created by a GW, and Inference of a GW's Momentum Flux from the Ion Vertical Displacement

We now review the mechanism by which a GW creates a TID. We then derive an expression for a GW's momentum flux at the observation altitude in terms of the TID properties and the Earth's magnetic field orientation.

4.1. Traveling Ionospheric Disturbance Created by a GW

The thermosphere is generally considered to begin just above the turbopause at $z \sim 107$ km, while the ionosphere is located above $z \geq 90$ km. As a GW propagates within the neutral thermosphere, the neutral molecules in the GW collide with the ions. The neutral wind perturbations associated with a GW push and pull the plasma along the Earth's magnetic field lines through ion drag, thereby creating a TID [*Klostermeyer*, 1972; *Yeh and Liu*, 1974; *Kirchengast et al.*, 1996; *Hocke and Schlegel*, 1996]. This plasma disturbance is not self-sustaining but relies on the GW for its maintenance.

In this section, we review the ion velocity perturbations induced by a GW following Appendix A in *Nicolls et al.* [2014]. We then compute the vertical displacement of the ions created by a GW. We assume that we are in the *F* region of the ionosphere, whereby a single ion, O^+, dominates (approximately $z > 200$ km) [*Banks and Kockarts*, 1973b, p. 131]. (Other ions important in the *D* and *E* regions of the ionosphere, N_2^+, O_2^+, and NO^+, can be taken into account via the inclusion of chemical reactions) [e.g., *Banks and Kockarts*, 1973b; *Yu et al.*, 2017].

If a GW propagates with an azimuth of ψ (clockwise from north), then

$$k = k_H \sin\psi, \quad l = k_H \cos\psi. \tag{29}$$

The corresponding wind velocity vector of this GW can be written as follows:

$$\mathbf{u}' = \left(u_0' \hat{i} + v_0' \hat{j} + w_0' \hat{k}\right) \exp(i\phi), \tag{30}$$

where u'_0, v'_0, and w'_0 are the zonal, meridional, and vertical velocity amplitudes, respectively; $\hat{i}$, $\hat{j}$, and $\hat{k}$ are the unit vectors in the geographic zonal (positive eastward), meridional (positive northward), and vertical (positive upward) directions, respectively; and ϕ is the phase of the GW:

$$\phi = kx + ly + mz - \omega_r t. \tag{31}$$

Note that u'_0 and v'_0 are in general complex in order to capture the phase difference between u' and w' and between v' and w'.

Because of neutral-ion collisions and because an ion can only easily move along the Earth's magnetic field, the induced ion velocity perturbation is approximately equal to the projection of the GW's velocity vector along the magnetic field. The unit vector along the magnetic field is

$$\hat{\mathbf{B}} = \cos\mathcal{I}\sin D\,\hat{i} + \cos\mathcal{I}\cos D\,\hat{j} - \sin\mathcal{I}\,\hat{k}, \tag{32}$$

where $\mathcal{I}$ is the dip or inclination angle and D is the magnetic declination angle (or the angle, positive eastward, between magnetic and geographic north). Here we define $\mathcal{I}$ positive down by convention in order to be consistent with the International Geomagnetic Reference Field (IGRF) model, whereas it was oppositely defined in *Nicolls et al.* [2014]. (For example, in the Northern (southern) Hemisphere $\hat{\mathbf{B}}$ points downward (upward) although $\mathcal{I} > 0$ ($\mathcal{I} < 0$) in the IGRF model. Thus, the results of *Nicolls et al.* [2014] can be applied here with the substitution $\mathcal{I} \to -\mathcal{I}$.) The ion velocity perturbation induced by a GW is then given by

$$\mathbf{v}'_i = v'_{i0}\exp(i\phi)\,\hat{\mathbf{B}}. \tag{33}$$

Here v'_{i0} is the ion velocity amplitude and is determined from equations (30) and (32):

$$v'_{i0} = \left(\mathbf{u}' \cdot \hat{\mathbf{B}}\right) / \exp(i\phi) = \cos\mathcal{I}\left(u'_0\sin D + v'_0\cos D\right) - w'_0\sin\mathcal{I}\ . \tag{34}$$

The vertical component of the induced ion velocity is

$$w'_i = w'_{i0}\exp(i\phi). \tag{35}$$

Using equations (32) and (33),

$$w'_i = \mathbf{v}'_i \cdot \hat{k} = -v'_{i0}\sin\mathcal{I}\exp(i\phi). \tag{36}$$

Therefore, the amplitude of the TID's vertical velocity is

$$w'_{i0} = -v'_{i0}\sin\mathcal{I}. \tag{37}$$

The vertical displacement of the ions during one quarter of a GW period is then

$$h_i = \int_0^{\tau_r/4} |w'_i|\mathrm{d}t = |\frac{\mathrm{e}^{i(kx+ly+mz)}w'_{i0}}{\omega_r}\exp(-i\omega_r t)|_0^{\tau_r/4} = \frac{|v'_{i0}\sin\mathcal{I}|\tau_r}{2\pi}. \tag{38}$$

h_i was previously determined from equation (28) and is shown in the last column of Table 1. Since τ_r is measured, we then determine the ion velocity amplitude, v'_{i0}, from equation (38). v'_{i0} will be used to determine the momentum flux of a GW at the observation altitude (see section 4.2).

4.2. Use of Vertical Ion Displacement to Infer the Momentum Flux of a GW at the Observation Altitude

In this section, we derive expressions for a GW's velocity and momentum flux at the observation (or measurement) altitude in terms of the vertical displacement of the ions, h_i, and the dip and declination angles of the Earth's magnetic field. These expressions will then be applied to the TIDDBIT data at the observation altitude, $z_{\rm obs}$, in section 5.1.

The zonal and meridional velocity amplitudes of a GW are

$$u'_0 = u'_{H0}\sin\psi, \quad v'_0 = u'_{H0}\cos\psi, \tag{39}$$

where u'_{H0} is the horizontal velocity amplitude and ψ is the azimuth. Plugging these into equation (34) and using equation (22), we obtain

$$v'_{i0} = u'_{H0}\cos\mathcal{I}(\sin\psi\sin D + \cos\psi\cos D) - w'_0\sin\mathcal{I} = u'_{H0}\left[\cos\mathcal{I}\cos(\psi - D) - \left(\tilde{w}_0/\widetilde{u_{H0}}\right)\sin\mathcal{I}\right]. \tag{40}$$

Here we calculate $(\tilde{w}_0/\widetilde{u_{H0}})$ from equation (12) at $z_{\rm obs}$. Plugging equation (40) into equation (38) and rearranging, the amplitude of the horizontal velocity of the GW is

$$\begin{aligned} u'_{H0} &= \frac{v'_{i0}}{|\,[\cos\mathcal{I}\cos(\psi-D)-\left(\tilde{w}_0/\widetilde{u_{H0}}\right)\sin\mathcal{I}]\,|}.\\ &= \frac{2\pi h_i}{\tau_r|\sin\mathcal{I}[\cos\mathcal{I}\cos(\psi-D)-\left(\tilde{w}_0/\widetilde{u_{H0}}\right)\sin\mathcal{I}]\,|}. \end{aligned} \tag{41}$$

The real component of the GW vertical velocity amplitude at $z_{\rm obs}$ is

$$|w'_0| = |u'_{H0}\left(\tilde{w}_0/\widetilde{u_{H0}}\right)|. \tag{42}$$

Then, the momentum flux *amplitude* of the GW at $z_{\rm obs}$ and time $t_{\rm obs}$ is

$$\left(u'_H w'\right)_0(z_{\rm obs}, t_{\rm obs}) = |u'_{H0}|\,|w'_0|, \tag{43}$$

where $|u'_{H0}|$ and $|w'_0|$ are determined from equations (41) and (42), respectively.

We utilize $(u'_H w')_0(z_{\rm obs}, t_{\rm obs})$ in our ray trace model to determine the GW momentum flux at all altitudes. This allows us to calculate the neutral perturbations (such as velocity and density) associated with this GW at all altitudes and times using equations (21)–(26).

5. Propagation and Dissipation of Observed GWs in the Thermosphere

5.1. Setup and Launch Values

In order to determine their amplitudes at higher altitudes, we ray trace the TIDDBIT GWs forward in time. We assume that these GWs are upward propagating at $z = z_{\rm obs}$. This is a reasonable assumption, because there are no known significant sources of GWs for $z > 283$ km. We include the errors in the horizontal wavelength and azimuth in the following manner; if a TIDDBIT GW has a horizontal wavelength of $\lambda_H = \overline{\lambda_H} \pm \Delta\lambda_H$ and an azimuth of $\theta = \bar{\theta} \pm \Delta\theta$, where overlines denote the measured values and $\Delta\lambda_H$ and $\Delta\theta$ denote the errors in λ_H and θ, respectively, then for this TIDDBIT GW we forward ray trace n^2 GWs having horizontal wavelengths and azimuths of

$$\lambda_H(i) = \overline{\lambda_H} + \Delta\lambda_H\left(-1 + \frac{2(i-1)}{n-1}\right) \text{ for } i = 1, 2, \ldots, n, \tag{44}$$

and

$$\theta(j) = \bar{\theta} + \Delta\theta\left(-1 + \frac{2(j-1)}{n-1}\right) \text{ for } j = 1, 2, \ldots, n, \tag{45}$$

respectively, where i and j are integers. Additionally, (1) if $\Delta\lambda_H \geq 0.9\overline{\lambda_H}$, we set $\Delta\lambda_H = 0.9\overline{\lambda_H}$ in equation (44) and (2) if $\Delta\theta \geq 180°$, we set $\Delta\theta = 180°$ in equation (45). In this paper, we set $n = 10$. This results in $n^2 = 100$ ray traced GWs for each TIDDBIT GW. For example, for TIDDBIT GW #1 with $\lambda_H = 174 \pm 28$ km and $\theta = -30° \pm 10°$ (see Table 1), we ray trace 100 GWs having all possible combinations of $\lambda_H = 146, 152, \ldots, 202$ km and $\theta = -40°, -38°, \ldots, -20°$.

We launch all GWs from 75.51°W, 38°N, $z_i = 220$ km and $t_i = 0400$ UT on 30 October 2007. Here we chose z_i significantly lower than the observation altitude $z_{\rm obs} = 283$ km because the ray traced GWs often cannot even propagate to $z = z_{\rm obs}$ using generally accepted atmospheric and damping parameters, and it is important to determine under what background conditions (e.g., temperature, wind, and viscosity) the GWs can propagate to $z_{\rm obs}$. For each GW, the launch value for λ_z is determined iteratively from equation (1) via calculating the solution for $\nu = 0$ as an initial guess then slowly increasing ν to the desired value. This results in the determination of λ_z for a GW rather than for an ordinary or extraordinary viscosity wave, since these waves also exist when viscous dissipation is strong [*Volland*, 1969; *Ma*, 2016]. (The occurrence of multiple values of λ_z at a given altitude when viscous dissipation is strong was noted in Figure 1 of *Vadas and Nicolls* [2009].)

We calculate the inclination and declination angles using the IGRF model with geodetic coordinates (i.e., the Earth is approximated as a spheroid). This model is available at http://www.ngdc.noaa.gov/geomag/magfield.shtml. At 75.51°W, 38°N and $z = 283$ km on 30 October 2007, $\mathcal{I} = 65.58°$ and $D = -10.75°$; thus, the magnetic field points westward and downward there. We set $(u'_H w')_0(\mathbf{x}_i, t_i) = 1$ at the launch then calculate $(u'_H w')_0(\mathbf{x}, t)$ at later times using equation (20). We dub these values the "unscaled" momentum fluxes.

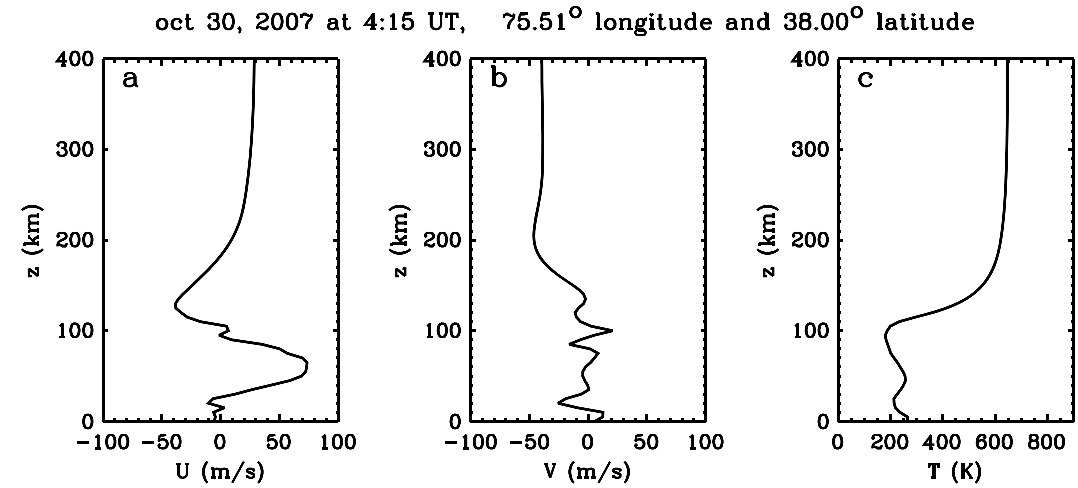

Figure 2. Background wind and temperature profiles at 75.51°W and 38°N on 30 October 2007 at 0415 UT. (a) Zonal velocity U. Positive is eastward. (b) Meridional velocity V. Positive is northward. (c) Temperature T.

If a GW then propagates to $z_{\rm obs}$, we multiply its unscaled momentum fluxes at all altitudes and times by $(u'_H w')_0(z_{\rm obs}, t_{\rm obs})$ (from equation (43)) divided by its unscaled momentum flux at $z_{\rm obs}$. This results in the correct momentum flux at all altitudes and times and equals $(u'_H w')_0(z_{\rm obs}, t_{\rm obs})$ at $z = z_{\rm obs}$.

The background atmosphere we use for ray tracing is constructed in the following manner. For $z \leq 25$ km, we utilize the European Centre for Medium-Range Weather Forecasts (ECMWF) ERA-Interim data from http://dss.ucar.edu. For $z \geq 35$ km, we utilize the standard resolution (5°) TIME-GCM data [*Roble and Ridley*, 1994] running at Atmospheric and Space Technology Research Associates [*Crowley et al.*, 2008, 2010]. We linearly interpolate the values for $25 \leq z \leq 35$ km. Figure 2 shows the background horizontal wind and temperature profiles from the combined ECMWF/TIME-GCM model on 30 October 2007 at 0415 UT. The horizontal wind at the highest altitude is primarily due to the migrating diurnal tide. At $z = 400$ km, it is southeastward, with a magnitude of ~48 m/s. Note that the horizontal wind is nearly constant for $z > 225$ km because of molecular viscosity and ion drag.

5.2. Forward Ray Tracing the TIDDBIT GWs

We now forward ray trace the TIDDBIT GWs (see Table 1) using the procedure outlined in section 5.1. We set the molecular viscosity to be

$$\mu = 3.34 \times 10^{-4} \bar{T}^{0.71} \text{ gm m}^{-1} \text{ s}^{-1} \tag{46}$$

[*Dalgarno and Smith*, 1962], which is the theoretically and empirically derived expression for atomic oxygen, the main molecular species in the thermosphere for $z > 200$ km. (See section 6 for the inclusion of all major species in the thermosphere.) This expression has been used previously for numerous GW studies [e.g., *Hickey and Cole*, 1988; *Vadas*, 2007]. We also set the Prandtl number to be $Pr = 0.7$ [*Kundu*, 1990]. Figure 3 shows the results. Blue to red colors in the color bar show the TIDDBIT wave # (see Table 1) from 1 to 10 having $\overline{\lambda_H} = 174$, 254, 177, 248, 186, 192, 568, 1077, 1599, and 1789 km, respectively. As mentioned previously, we ray trace 100 GWs for each TIDDBIT GW in order to include the error bars in λ_H and θ. Figure 3a shows the initial horizontal phase speed c_H as a function of the initial azimuth θ. Most of the GWs propagate northwestward or northward with $c_H \sim 100$–700 m/s. The altitude where $(\overline{u'_H w'})$ is maximum is defined as $z_{\rm diss}$ and is shown in Figure 3b as a function of the initial θ. We see that $z_{\rm diss} \sim 220$–260 km. We calculate u'_H along each GW's raypath using equations (21) and (22). The altitude where u'_H is maximum is shown in Figures 3c–3e as functions of the initial c_H, θ, and λ_H, respectively. Figure 3f shows the altitude where u'_H is a maximum as a function of $|\lambda_z|$ at the location and time where u'_H is maximum. The GWs which have maxima at $z \sim 240$–260 km tend to be northwestward propagating and have relatively large values of $|\lambda_z|$. From Figure 2, these GWs are propagating against the background wind, which causes $|\lambda_z|$ to increase [*Hines*, 1960; *Yeh et al.*, 1975; *Fritts and Vadas*, 2008]. Importantly, *none* of the GWs have u'_H maximum for $z > 265$ km and therefore could not have created a horizontal wind peak at $z \sim 325$ km.

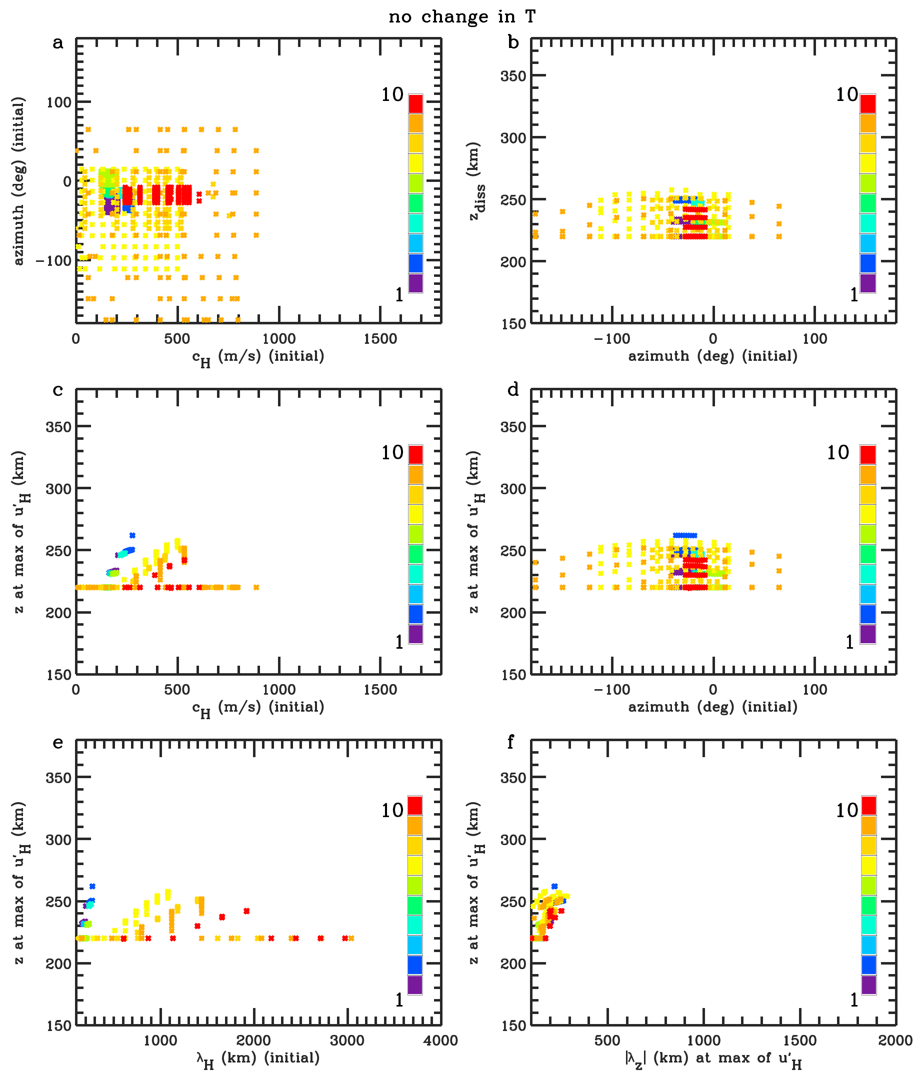

Figure 3. Forward ray trace results for the 10 TIDDBIT GWs through background temperatures and densities given by ECMWF/TIME-GCM. (a) c_H (initial) versus θ (initial). (b) θ (initial) versus $z_{\rm diss}$ (i.e., the altitude where $u'_H w'$ is maximum). (c) c_H (initial) versus the altitude where the amplitude of u'_H is maximum. (d) Same as Figure 3c but as a function of θ (initial). (e) Same as Figure 3c but as a function of λ_H (initial). (f) Same as Figure 3c but as a function of $|\lambda_z|$ calculated where u'_H is maximum. The dark blue to red colors in the color bar denote the TIDDBIT wave # from 1 to 10 in Table 1.

Figure 3 points out a serious concern: namely, that all (except for possibly one) of these TIDDBIT GWs could not have been observed at $z = z_{\rm obs}$ because their amplitudes would have been too small at that altitude. This is because $z_{\rm diss} \sim 230-250$ km for all but one of the TIDDBIT GWs in Figure 3b (and for that TIDDBIT GW, there are only a few out of 100 possibilities for which $z_{\rm diss} \sim 250-260$ km). Since a GW's amplitude is extremely small (insignificant) at $z_{\rm diss} + H$, using $H \sim 27-30$ km at $z = 230-250$ km (from the TIME-GCM), the GWs with $z_{\rm diss} \sim 230-250$ km would have insignificant (undetectable) amplitudes at $z \sim z_{\rm diss} + H \sim 257-280$ km. Therefore, Figure 3 highlights the existence of a serious discrepancy between current GW dissipative theory and the TIDDBIT/rocket observations.

If we double (quadruple) the neutral background winds, we find that the altitude where u'_H is maximum increases to $z \simeq 270$ km ($z \simeq 275$ km) (not shown); however, these altitudes are still significantly lower than $z_{\rm obs}$ and $z \sim 325$ km. Therefore, doubling or quadrupling the background winds does not resolve the serious discrepancy between GW dissipative theory and observations.

5.3. Possible Reasons for the Serious Discrepancy Between Theory and Data

There are several reasons that the ray traced GWs might not have propagated as high as was detected that evening. One possible reason is that the background temperature $\bar{T}$ used for ray tracing might not have been as large as the actual $\bar{T}$ that evening. This is because a larger $\bar{T}$ results in a larger $\bar{\rho}$ at a given altitude z, which corresponds to a smaller $\nu = \mu/\bar{\rho}$. A smaller ν then allows a GW to propagate higher in the thermosphere before dissipating [*Vadas*, 2007].

We investigate the possibility that $\bar{T}$ from the combined ECMWF/TIME-GCM model might have been smaller than the actual $\bar{T}$ that evening. Figure 4 shows $\bar{T}$ on 30 October 2007 from the TIME-GCM (ASPEN) and the NRLMSISE-00 (Mass Spectrometer Incoherent Scatter (MSIS)) empirical model [*Picone et al.*, 2002] as a function of time at Millstone Hill. (Millstone Hill is the location of the Massachusetts Institute of Technology Haystack Observatory in Massachusetts at 42.6°N and −71.5°W and is ∼650 km NE of Wallops Island.) For both models, the diurnal tide is clearly visible in $\bar{T}$ for $z > 200$ km. At $z = 300$ km, the MSIS $\bar{T}$ is ∼50–90 K higher than the TIME-GCM $\bar{T}$ at 0400–0700 UT. Figure 5 shows $\bar{T}$ a few days later on 2 November 2007 at Millstone Hill. Again, the MSIS $\bar{T}$ is ∼50–90 K higher than the TIME-GCM $\bar{T}$ at 0400–0700 UT. We also show the Millstone Hill ion temperatures, T_i, on 2 November 2007 in Figure 5. We assume that $T_i \simeq \bar{T}$. This assumption is reasonable, since *Conde and Nicolls* [2010] found that T_i and $\bar{T}$ agree reasonably well over short time periods for long-term data sets at Poker Flat, Alaska [*Nicolls et al.*, 2012]. Although the Millstone Hill T_i data are scattered at 300 km, it is clear that the TIME-GCM $\bar{T}$ are ∼30–60 K lower than T_i during 0400–0700 UT. The conclusion from Figures 4 and 5 is that $\bar{T}$ from the TIME-GCM might be ∼30–90 K lower than the actual $\bar{T}$ at $z = z_{\rm obs}$ at Wallops Island on 30 October 2007. We will investigate how an increase in $\bar{T}$ by ∼30–90 K affects the ray trace results in section 5.4.

Another possible reason that the GWs might not have propagated as high as was observed is that the molecular viscosity μ given by equation (46) is too large in the middle to upper thermosphere. Indeed, *Vadas* [2007] performed GW ray race studies using μ from equation (46) and calculated λ_z as a function of altitude. They found that the GW ray trace results agreed reasonably well with Arecibo Observatory and Middle and Upper (MU) atmosphere radar data up to $z \sim 225$ km (see Figure 11 of that paper). Additionally, fair agreement was found between GW theory and 630 nm airglow data at $z \simeq 250$ km over Alaska [*Nicolls et al.*, 2012]; however, independent λ_H measurements were not available in that study. Therefore, in our opinion, equation (46) is essentially untested with data for $z > 250$ km to our knowledge.

We now investigate the possibility that μ given by equation (46) may be too large in the middle to upper thermosphere. Equation (46) is a theoretical/empirical formula which was derived by *Dalgarno and Smith* [1962] via taking into account the viscous interactions between atomic oxygen when their separation distances were of order 10 to a few tens of atomic units (AU). Here 1 AU $= 5.3 \times 10^{-11}$ m is an atomic unit. To estimate the applicability of this formula in the thermosphere, we calculate the separation distances between molecules at various altitudes.

In the Earth's atmosphere, the average number of molecules per unit volume is

$$n = \bar{\rho} N_A / X_{\rm MW}, \tag{47}$$

where $N_A = 6.02 \times 10^{23}$ molecules/mol is Avogadro's number and the average distance between molecules is

$$d \simeq \frac{1}{n^{1/3}}. \tag{48}$$

Additionally, the mean free path (i.e., the average distance traveled between collisions) is

$$\Lambda \sim \frac{1}{n\sigma_0}, \tag{49}$$

where σ_0 is the collisional cross section and is $\sigma_0 = 5 \times 10^{-15}$ cm^2 for atomic oxygen, assuming a rigid sphere approximation [*Banks and Kockarts*, 1973a, p. 187]. At $z = 100$ km, typical parameters are $\bar{\rho} \sim 5 \times 10^{-4}$ to 10^{-3} g/m^3, $\bar{T} \sim 150 - 200$ K and $X_{\rm MW} \sim 29$ g/mol. Then, $n \sim 2 \times 10^{18}$–2×10^{19} molecules/m^3 and $d \sim$ 7000–15,000 AU from equations (47) and (48). From the ideal gas law $\bar{p} = R\bar{\rho}\bar{T}$, the pressure is $\bar{p} \sim$ 20–100 gm/m/s^2. Using equation (49), the mean free path is relatively small: $\Lambda \sim$ 0.1–1 m.

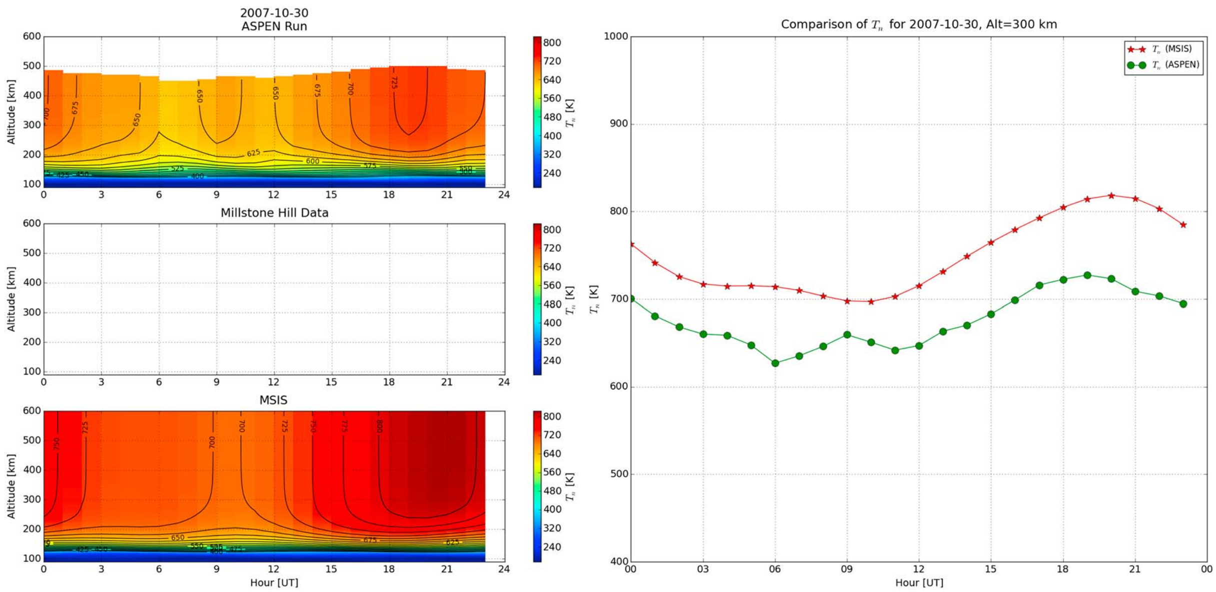

Figure 4. Background temperatures on 30 October 2007 at Millstone Hill. (left column) TIME-GCM (ASPEN) neutral temperature, Millstone Hill ion temperature data (not available this evening), and MSIS neutral temperature. (right) A comparison of these temperatures at $z = 300$ km. The red stars show the MSIS data, and the green dots show the ASPEN data.

At $z = 250$ km, the background density is significantly smaller: $\bar{\rho} \sim 10^{-8}$–10^{-7} g/m^3. Additionally, $\bar{T} \sim 600$–1500 K, $X_{\mathrm{MW}} \sim 18$–20 g/mol, and $\bar{p} \sim 0.0025$–0.07 gm/m/s^2. Therefore, $n \sim 3 \times 10^{14}$–3×10^{15} molecules/m^3 from equation (47), and the average distance between molecules is $d \sim 130{,}000$–$270{,}000$ AU from equation (48). This distance is much larger than the interaction distance in *Dalgarno and Smith* [1962]. Additionally, the mean free path is $\Lambda \sim 1$–6 km from equation (49), which is quite large. At higher altitudes, the background density is even smaller, which results in even larger values of d and Λ.

Figures 6a and 6b show d and Λ at Wallops Island on 30 October 2007 at 0415 UT using the background atmosphere from Figure 2. At $z \sim 200$–300 km, $d \sim 100{,}000$–$300{,}000$ AU and $\Lambda \sim 0.5$–8 km. Thus, the average distance between molecules is much larger than the separation distance used to derive equation (46).

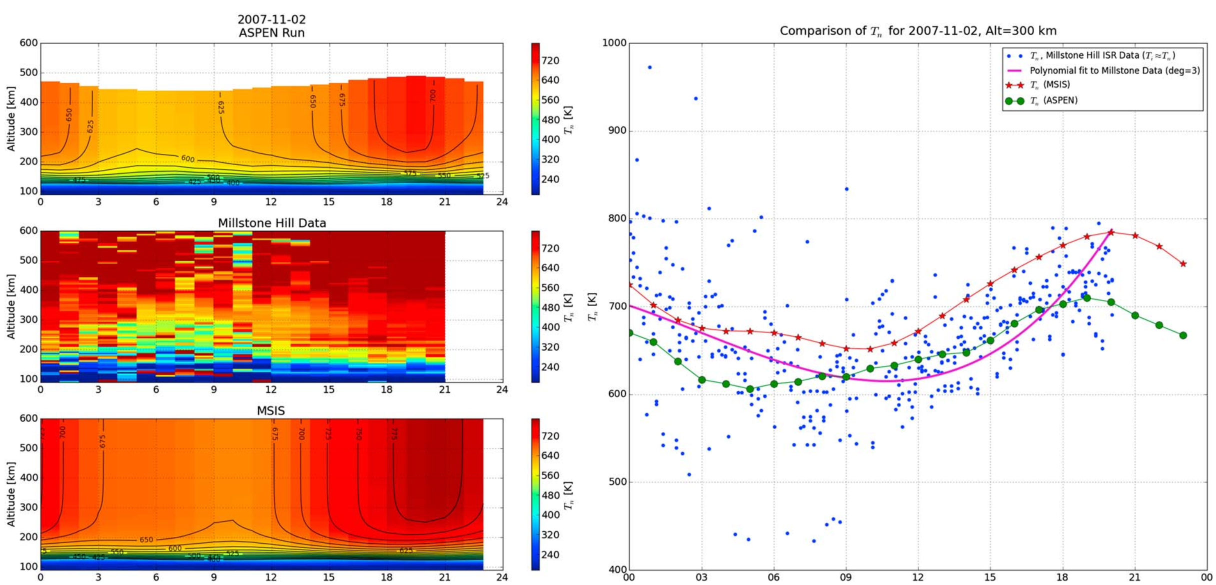

Figure 5. Same as in Figure 4 but for 2 November 2007. Additionally, the blue dots show the Millstone Hill T_i data, and the purple line shows a polynomial fit to the Millstone Hill data.

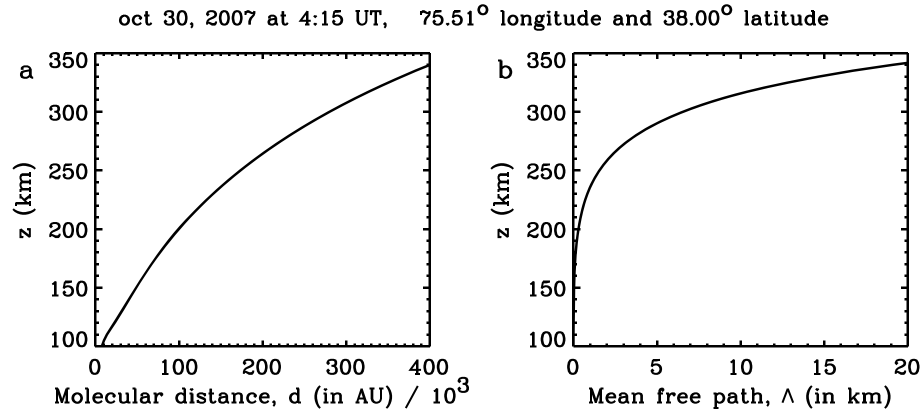

Figure 6. (a) Average molecular distance d (in AU) divided by 10^3 as a function of altitude at 75.51°W and 38°N on 30 October 2007 at 0415 UT. (b) Corresponding mean free path Λ (in km).

Therefore, it is possible that equation (46) is not applicable for $z > 225$ km because the background pressure and density are too small there.

Because $\bar{p} = R\bar{\rho}\bar{T}$, a fluid can have a large $\bar{T}$ with extremely small values of $\bar{\rho}$ and $\bar{p}$. Indeed, in the limit that $\bar{\rho}$ and $\bar{p}$ go to zero for a fixed $\bar{T}$, it seems self-evident that equation (46) cannot be correct (i.e., that μ only depends on $\bar{T}$ and not on the separation distance between molecules), because the distance between molecules $\rightarrow \infty$, and therefore no collisions can occur. No collisions means that the molecular viscosity μ must $\rightarrow 0$. Therefore, it seems self-evident that μ must decrease somewhere in the middle to upper thermosphere. We hypothesize that μ depends on the inverse distance between molecules to some power for extremely small values of $\bar{\rho}$ and $\bar{p}$ in the middle to upper thermosphere. We investigate how a decrease of μ in the middle to upper thermosphere affects the ray trace results in section 5.5.

Finally, it is also possible that the u'_H peak observed by the rocket at $z \simeq 325$ km was created by GWs that were outside the field of view observed by TIDDBIT, since GWs propagate horizontally and vertically at the same time. We now investigate this possibility. The vertical distance between $z_{\rm obs}$ and $z \simeq 325$ km is $\Delta z \simeq 40$ km. Since a GW's intrinsic frequency (neglecting dissipation) is approximately

$$\omega_{Ir} \sim N_B \cos\xi \tag{50}$$

[*Vadas et al.*, 2009, equation (19)], where ξ is the angle of the GW's raypath from the zenith (i.e., vertical), the horizontal distance traveled by a GW with $\omega_{Ir} << N_B$ is

$$\Delta x_L \simeq \frac{\tau_{Ir}}{\tau_B}\Delta z, \tag{51}$$

where $\tau_B = 2\pi/N_B$ is the buoyancy period and $\tau_{Ir} = 2\pi/\omega_{Ir}$ is the intrinsic GW period. Since $\tau_B \sim 10$–15 min at $z \sim 300$ km, we estimate horizontal propagation distances of $\Delta x_L \sim 60$–240 km for GWs having intrinsic periods of $\tau_{Ir} \simeq 15$–60 min that propagate $\Delta z = 40$ km vertically. (These periods roughly correspond to the TIDDBIT GW periods in Table 1.) The horizontal extent of the TIDDBIT array is about 150 km, with reflection points separated by about 75 km. The rocket observations at $z = 325$ km were made about 100 km SE of the TIDDBIT field of view. Given horizontal propagation distances of $\Delta x_L \sim 60$–240 km and that $|\lambda_z| > 50$ km for most of the GWs (see Figure 3f), it seems likely that northwestward propagating GWs observed by the rocket would also be within TIDDBIT's field of view. Therefore, it is unlikely that the horizontal wind peak at $z \sim 325$ km observed by the rocket was due to a GW that TIDDBIT did not observe.

5.4. Ray Trace Sensitivity Studies for Increasing $\bar{T}$

We now estimate how much $\bar{T}$ needs to be increased by in order for the ray trace results to approximately agree with the rocket data. For these studies, we define $\bar{T}$ in the thermosphere via the following idealized function:

$$\bar{T}(x,y,z,t) = \bar{T}_{\rm original}(x,y,z,t)\left[1 + \alpha\tanh\left(\frac{(z - z_{\rm inc})}{\Delta z_{\rm inc}}\right)\right], \tag{52}$$

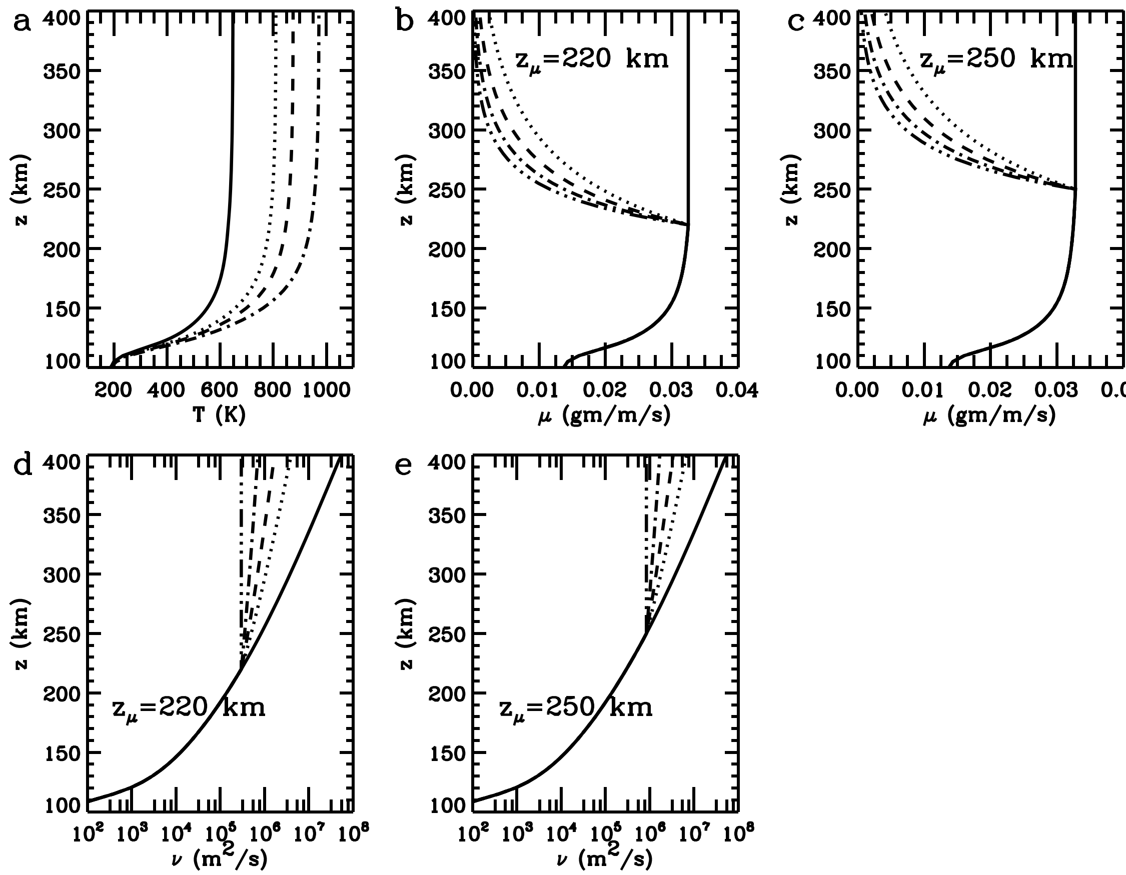

Figure 7. (a) Background temperature $\bar{T}$ at 75.51°W and 38°N on 30 October 2007 at 0415 UT using equation (52). The solid, dotted, dashed, and dash-dotted lines show $\alpha = 0$, 0.25, 0.35, and 0.5, respectively. (b) The molecular viscosity μ (in gm/m/s) at the same location and time as in Figure 7a using equation (53) with $z_\mu = 220$ km. The solid, dotted, dashed, dash-dotted, and dash-dot-dot-dot lines show $\beta = 0$, 1.5, 2, 2.5, and 3, respectively. (c) Same as Figure 7b but for $z_\mu = 250$ km. (d) Same as Figure 7b but showing the kinematic viscosity ν (in m^2/s). (e) Same as Figure 7d but for $z_\mu = 250$ km.

where $\bar{T}_{\text{original}}(x, y, z, t)$ is the temperature profile from the combined ECMWF/TIME-GCM model, α is a constant, $z_{\text{inc}} = 100$ km, and $\Delta z_{\text{inc}} = 50$ km. The exospheric temperature is then $\bar{T}_{\text{original}}(z = \infty)(1 + \alpha)$. Note that $\bar{T}_{\text{original}}(\infty) \sim 650$ K at 0415 UT on 30 October 2007 from Figure 2c. Figure 7a shows the background temperature profiles for $\alpha = 0.25, 0.35$, and 0.5, corresponding to a 25, 35, and 50% temperature increase, respectively. We recalculate the background density and pressure using these new temperature profiles and utilize the background winds from the combined ECMWF/TIME-GCM model. We then ray trace all GWs through these atmospheres. Figure 8 shows the altitude where u'_H is a maximum as functions of the initial c_H and λ_H. As α and $\bar{T}(\infty)$ increase, the altitudes where u'_H is maximum increases. For $\alpha = 0.25$ (for which $\bar{T}(\infty) \sim 810$ K), a few large-scale GWs have their u'_H maxima at $z \simeq 300$ km, although no GW has its u'_H maximum at $z > 310$ km. For $\alpha = 0.35$ (for which $\bar{T}(\infty) \sim 875$ K), many GWs have their u'_H maxima at $z \sim 310$–335 km. This occurs for GWs #7–10 having $\lambda_H \sim 900$–2200 km, $c_H \sim 400$–700 m/s, and $\theta \sim -180$ to 20° (not shown). Note that the altitude where u'_H is maximum is relatively insensitive to the azimuth (not shown) because the background wind is small compared to the GW horizontal phase speeds. Finally, for $\alpha = 0.50$ (for which $\bar{T}(\infty) \sim 970$ K), there are tens of GWs with u'_H maximum at $z \sim 310$–370 km. Again, these are GWs #7–10. Thus, in order to have one or two GWs with u'_H maxima at $z \sim 325$ km, we require $\alpha \simeq 0.35$ or $\bar{T}(\infty) \simeq 875$ K, which is $\simeq 225$ K larger than $\bar{T}$ from the TIME-GCM. This temperature difference is much larger than the likely discrepancy of ~30–90 K estimated in section 5.3. Therefore, it is unlikely that a somewhat smaller-than-actual model $\bar{T}$ is responsible for the fact that none of the ray traced GWs in Figure 3 had their u'_H maxima at $z \sim 325$ km.

5.5. Ray Trace Sensitivity Studies for Decreasing μ

We now estimate how much μ needs to be decreased in the middle to upper thermosphere in order for the ray trace results to approximately agree with the rocket data. We assume that in this region of the atmosphere, μ

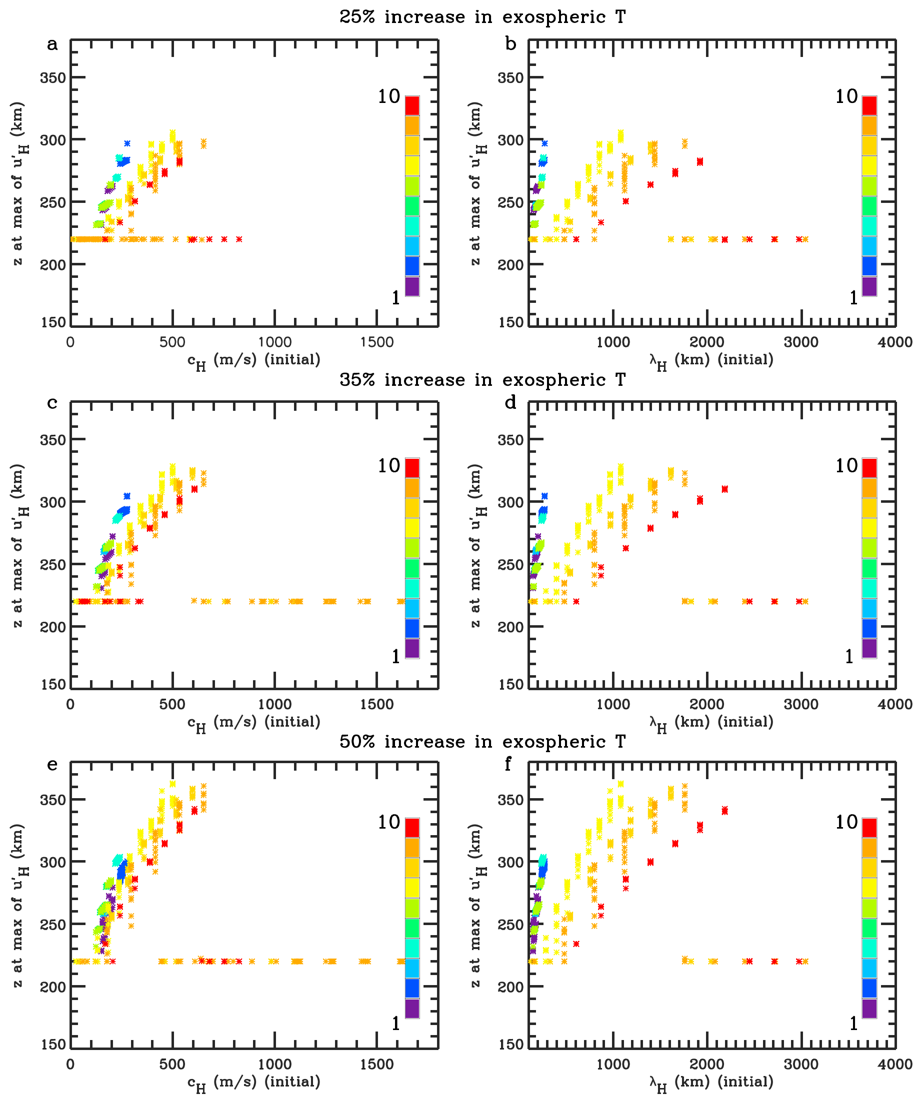

Figure 8. Forward ray trace results for the 10 TIDDBIT GWs through background temperatures given by equation (52). (a) c_H (initial) versus the altitude where u'_H is maximum for $\alpha = 0.25$. (b) Same as in Figure 8a but as a function of λ_H (initial). (c and d) Same as in Figures 8a and 8b except for $\alpha = 0.35$. (e and f) Same as in Figures 8a and 8b except for $\alpha = 0.5$. The dark blue to red colors denote the TIDDBIT wave # from 1 to 10 in Table 1.

depends on the inverse of d to an unknown (to-be-determined) power β, namely, $\mu \propto 1/d^\beta$. Because $d \propto 1/\bar{\rho}^{1/3}$ from equations (47) and (48), we assume an idealized functional form for μ of

$$\mu = \begin{cases} 3.34 \times 10^{-4} \bar{T}^{0.71}\ \mathrm{gm\,m^{-1}\,s^{-1}} & \text{for} \quad z < z_\mu \\ \mu(z_\mu) \left(\dfrac{\bar{\rho}}{\bar{\rho}(z_\mu)} \right)^{\beta/3} & \text{for} \quad z \geq z_\mu, \end{cases} \tag{53}$$

where z_μ is the altitude where μ begins to decrease from its value given by equation (46) and $\mu(z_\mu)$ is the value of μ at $z = z_\mu$. We utilize the background temperature and wind from the combined ECMWF/TIME-GCM model described in section 5.1. Figures 7b and 7c show μ as a function of altitude for $\beta = 0$, 1.5, 2, 2.5, and 3. Here we show $z_\mu = 220$ and 250 km, because the observational data agree reasonably well with μ using equation (46) for $z < 225$ km [*Vadas*, 2007]. Although we do not show the corresponding μ profiles here, we also ray trace the GWs using $z_\mu = 270$ km in order to constrain the final results (see below). Note that it is not useful to choose $z_\mu \geq 283$ km, because then nearly all of the TIDDBIT GWs would not have been observed (see section 5.2). Figures 7d and 7e show ν as a function of altitude for $\beta = 0$, 1.5, 2, 2.5, and 3. Except for

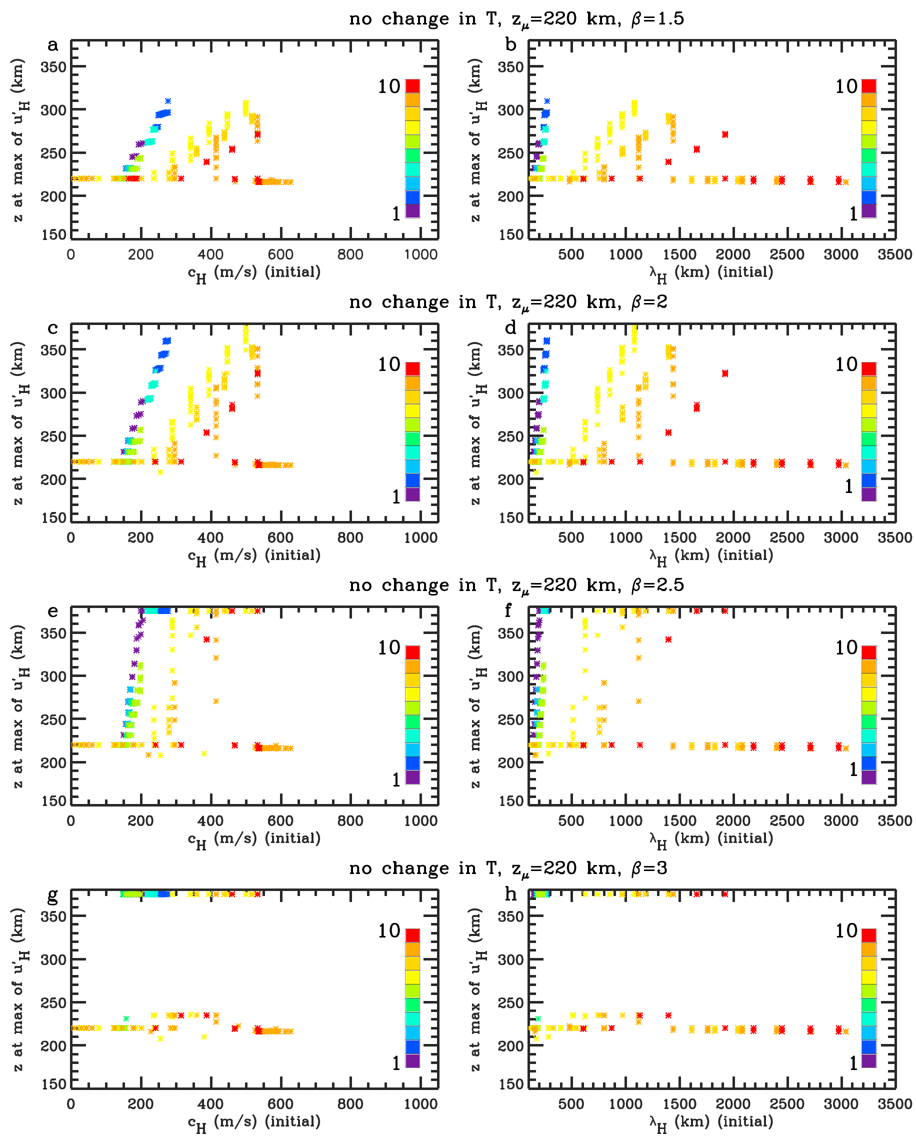

Figure 9. Forward ray trace results for the 10 TIDDBIT GWs through background temperatures given by the ECMWF/TIME-GCM model described in section 2.1. μ is given by equation (53) with $z_\mu = 220$ km. (a) c_H (initial) versus the altitude where the amplitude of u'_H is maximum for $\beta = 1.5$. (b) Same as Figure 9a but as a function of λ_H (initial). (c–h) Same as Figures 9a and 9b except that $\beta = 2$ (Figures 9c and 9d), $\beta = 2.5$ (Figures 9e and 9f), and $\beta = 3$ (Figures 9g and 9h). The dark blue to red colors denote the TIDDBIT wave # from 1 to 10 in Table 1.

$\beta = 3$, ν increases with altitude for all of the profiles; therefore, molecular viscosity and thermal diffusivity will eventually dissipate every upward propagating GW in the middle to upper thermosphere even if μ decreases with altitude above z_μ.

We ray trace all GWs through the background atmosphere with $\beta = 1.5$, 2, 2.5, and 3. Figure 9 shows the results for $z_\mu = 220$ km. If the altitude where u'_H is maximum is at $z > 375$ km, we show the GW at $z = 375$ km in order to emphasize that the GW dissipates above $z = 375$ km. As β increases to 2.5, ν increases less quickly with altitude than for μ constant, thereby allowing the GWs to penetrate to higher altitudes prior to dissipating. (However, for $\beta = 3$, $\nu \sim$ constant in the middle to upper thermosphere (see Figure 7).) This results in a significant increase in the altitudes where u'_H are maximum. Although $\beta = 1.5$ does not result in any GWs having their u'_H maximum at $z \sim 325$ km, $\beta = 2 - 2.5$ likely results in several GWs having their u'_H maxima at $z \simeq 325$ km. Note that $\beta = 3$ results in too many GWs having their u'_H maximum at $z \gg 325$ km (which is not observed in the rocket data). Figure 10 shows the results for $z_\mu = 250$ km. These results are similar to Figure 9 except that several GWs likely have their u'_H maximum at $z \sim 325$ km for $\beta = 2.5$. However, we note that many

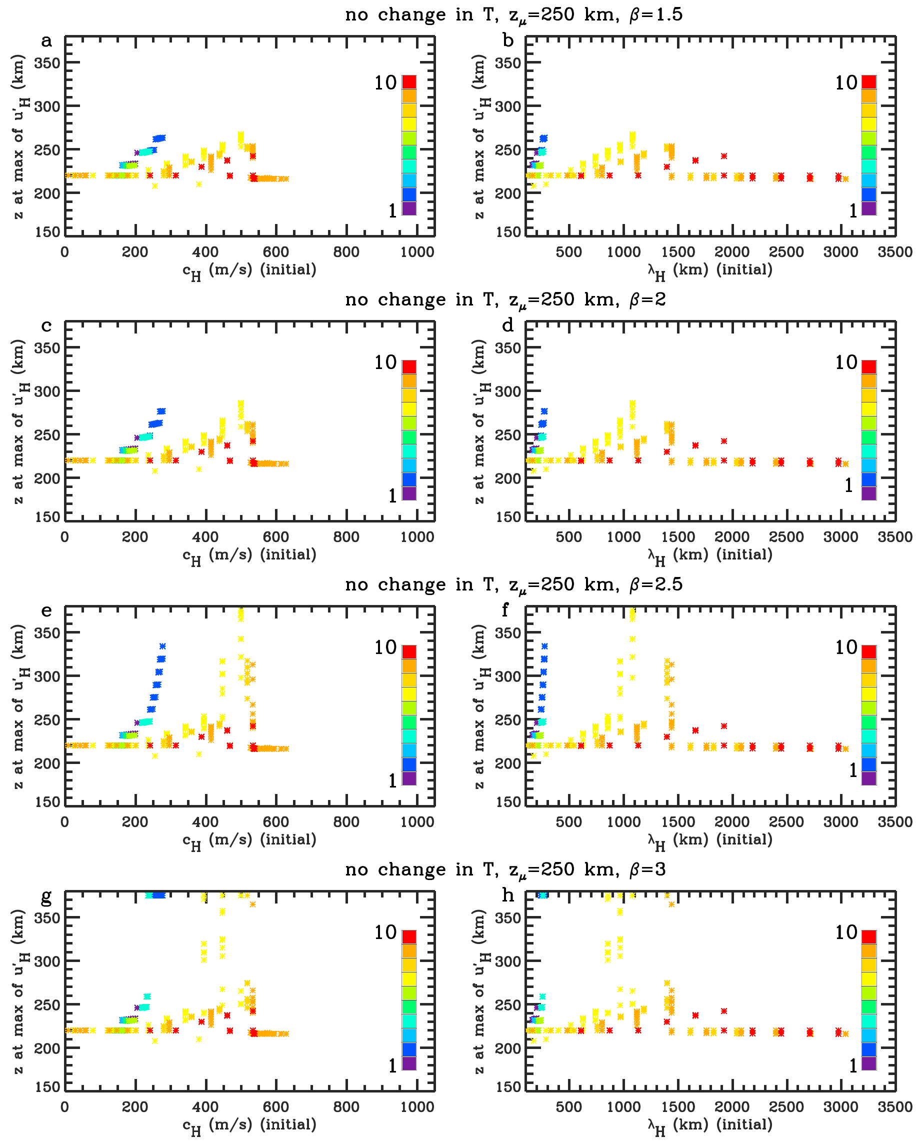

Figure 10. Same as in Figure 9 except for $z_\mu = 250$ km.

of the GWs having their u'_H maximum at $z \sim 325$ km have residues somewhat >1 (not shown). While the WKB theory might still give reasonable solutions in this transition regime, it does indicate that strong dissipation is likely occurring for these GWs. Figure 11 shows the results for $z_\mu = 270$ km. In this case, no GWs have their u'_H maximum at $z \sim 325$ km. If we select $z_\mu = 220$ km as the "most probable" altitude above which μ decreases, these results suggest that $\beta = 2$ and $\mu \propto \bar{\rho}^{0.67}$ (i.e., $\mu \propto 1/d^2$) at $z \geq 220$ km. We will further constrain this conclusion via calculating the magnitude of u'_H at their maxima in section 5.6.

5.6. GW Velocity and Density Perturbations Above the Measurement Altitude

In this section, we calculate the wind and density perturbations associated with those GWs having u'_H maxima at $300 \leq z \leq 350$ km. We use the results from Figures 9e and 9f for $z_\mu = 220$ km and $\beta = 2$. We do not use the $z_\mu = 250$ km results because they do not result in u'_H amplitudes that are large enough for GWs with residues <1 (not shown). Figures 12a and 12b show the values of u'_H at the altitudes where u'_H is maximum as functions of (a) the initial λ_H and (b) θ evaluated where u'_H is a maximum, respectively. Large amplitudes of $u'_H \sim 20-80$ m/s are obtained for $\lambda_H \sim 600-1600$ km. These correspond to the TIDDBIT GWs with $\tau_r = 36-60$ min. At $\theta \sim -45°$ (corresponding to the angle of the wind measured by the rocket at $z \sim 325$ km assuming zero vertical wind (see Figure 1b)), $u'_H \sim 30-50$ m/s. Since the TIDDBIT GWs are high frequency, their horizontal wind vectors are parallel to their propagation direction. Thus, it is possible that

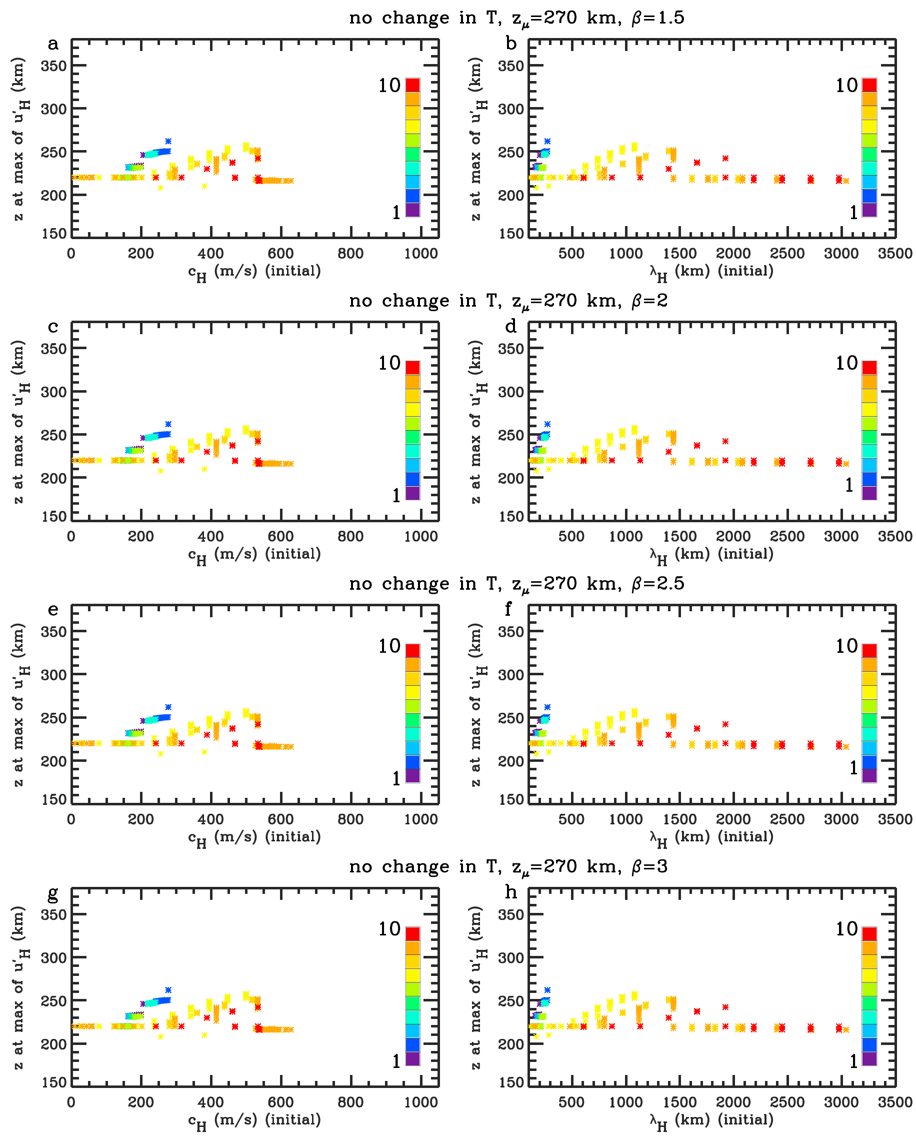

Figure 11. Same as in Figure 9 except for $z_\mu = 270$ km.

constructive interference of a few of the TIDDBIT GWs could, in principle, account for the ∼100 m/s horizontal wind peak seen in Figure 1a.

The large values of u'_H at $\theta \sim -90°$ in Figure 12b occurs for those GWs that propagate nearly perpendicular to the magnetic field. These GWs create very small-amplitude TIDs because $\mathbf{u}' \cdot \hat{\mathbf{B}} \sim 0$ or $v'_{i0} \sim 0$ from equation (34). However, because the TIDDBIT GWs had moderate amplitudes of $h_i \sim 0.1-1$ km (see Table 1), a TID having $\theta \sim -70°$ and a moderate amplitude could only have been created by a GW with a very large value of u'_H (see equation (41)). This is why $u'_H \to \infty$ at the azimuth where $\mathbf{u}' \cdot \hat{\mathbf{B}} \to 0$ in Figure 12b. Figure 12c shows the GW vertical velocities at the altitude where u'_H is maximum. These velocities range from $w' \sim 2-18$ m/s and are largest for those GWs propagating nearly perpendicular to the magnetic field: $w' \sim 13-15$ m/s. Thus, the vertical wind component for these GWs is not negligible. Therefore, if the peak at $z \sim 325$ km in Figure 1a was caused by these GWs, it may not have been reasonable to assume that the vertical wind component was negligible. Figure 13d shows $\rho'/\bar{\rho}$ (using equation (26)) at the altitude where u'_H is maximum. The density perturbations range from $\rho'/\bar{\rho} \sim 1$ to 10%.

Figure 13 shows the same results, but for $\beta = 2.5$. The wind peaks are smaller here, with $u'_H \sim 5-35$ m/s, $w' \sim 2-8$ m/s, and $\rho'/\bar{\rho} \sim 1$ to 4%.

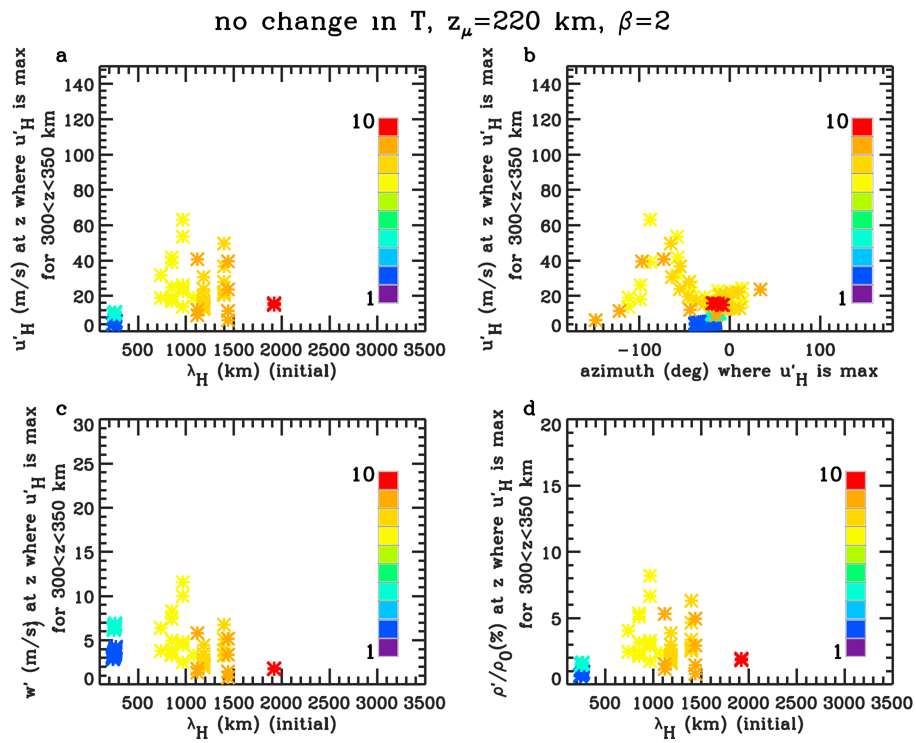

Figure 12. Forward ray trace results for the 10 TIDDBIT GWs where the background is given by the combined ECMWF/TIME-GCM model. The molecular viscosity μ is given by equation (53) with $z_\mu = 220$ km and $\beta = 2$. Only those GWs with u'_H maximum at $300 \le z \le 350$ km are shown. (a) λ_H (initial) versus u'_H at the altitude where u'_H is maximum. (b) Same as Figure 12a but x axis displays θ at the location where u'_H is maximum. (c) λ_H (initial) versus w' at the altitude where u'_H is maximum. (d) Same as Figure 12a but the y axis displays $\rho'/\bar{\rho}$ (in %) at the altitude where u'_H is maximum.

Therefore, we conclude that $z_\mu \simeq 220$ km and $\beta = 2$ enables GWs to easily propagate to $z_{\rm obs}$ and result in u'_H peaks that agree reasonably well with the rocket data. These values imply a dependence for μ at $z \ge z_\mu$ of

$$\mu \propto \bar{\rho}^{0.67} \quad \text{or} \quad \mu \propto \frac{1}{d^2}. \tag{54}$$

Using the background atmosphere for the combined ECMWF/TIME-GCM model along with $z_\mu = 220$ km and $\beta = 2$, we examine the GWs shown in Figure 12 for which the maxima of u'_H occurred for $320 \le z \le 350$ km and $-80° \le \theta \le -10°$. TIDDBIT GWs #2, 4, 7, 8, and 10 contributed. However, $u'_H \le 20$ m/s for GWs #2, 4, and 10, which are much smaller than the wind peak measured by the rocket. On the other hand, TIDDBIT GWs #7 and 8 have much larger amplitudes of $u'_H \sim 20$ to hundreds of m/s. Therefore, we only show examples of TIDDBIT GWs #7 and 8 here.

Figure 14a shows the magnitudes of u'_H, w', and $\rho'/\bar{\rho}$ as functions of altitude for TIDDBIT GW #7 having launch values (at $z = z_i$) of $\lambda_H = 850$ km, $\theta = -65°$, and $\tau_{lr} = 31$ min. (Note that the phases of the GW are not included here.) The maxima occur at $z \sim 335$ km with $u'_H \sim 125$ m/s, $w' \sim 26$ m/s, and $\rho'/\bar{\rho} \sim 15\%$. Note that the ray trace solutions may not be valid above the diamonds, because the residue is greater than 1 there [*Einaudi and Hines*, 1970; VF05]. Figure 14b shows the results for TIDDBIT GW #7 having launch values of $\lambda_H = 900$ km, $\theta = -60°$, and $\tau_{lr} = 33$ min. The maxima occur at $z \sim 330$ km with $u'_H \sim 40$ m/s, $w' \sim 8$ m/s, and $\rho'/\bar{\rho} \sim 5\%$. Figure 14c shows the results for TIDDBIT GW #7 having launch values of $\lambda_H = 1000$ km, $\theta = -65°$, and $\tau_{lr} = 35$ min. Here the maxima occur at $z \sim 335$ km with $u'_H \sim 60$ m/s, $w' \sim 10$ m/s, and $\rho'/\bar{\rho} \sim 7\%$. Figure 14d shows the results for TIDDBIT GW #8 having launch values of $\lambda_H = 1200$ km, $\theta = -60°$, and $\tau_{lr} = 39$ min. The maxima occur at $z \sim 330$ km with $u'_H \sim 40$ m/s, $w' \sim 6$ m/s, and $\rho'/\bar{\rho} \sim 5\%$. Note from Figure 14 that the largest values of u'_H occur for the GWs that propagate nearly perpendicular to the Earth's magnetic field. Note that in all cases the GW amplitudes (u'_H, w', and ρ'/ρ) go rapidly to zero above $z \sim 350$ km.

We conclude from Figure 14 that it is possible that TIDDBIT GWs #7 and #8 caused the u'_H peak in Figure 1a at $z \sim 325$ km for $z_\mu = 220$ km and $\beta = 2$.

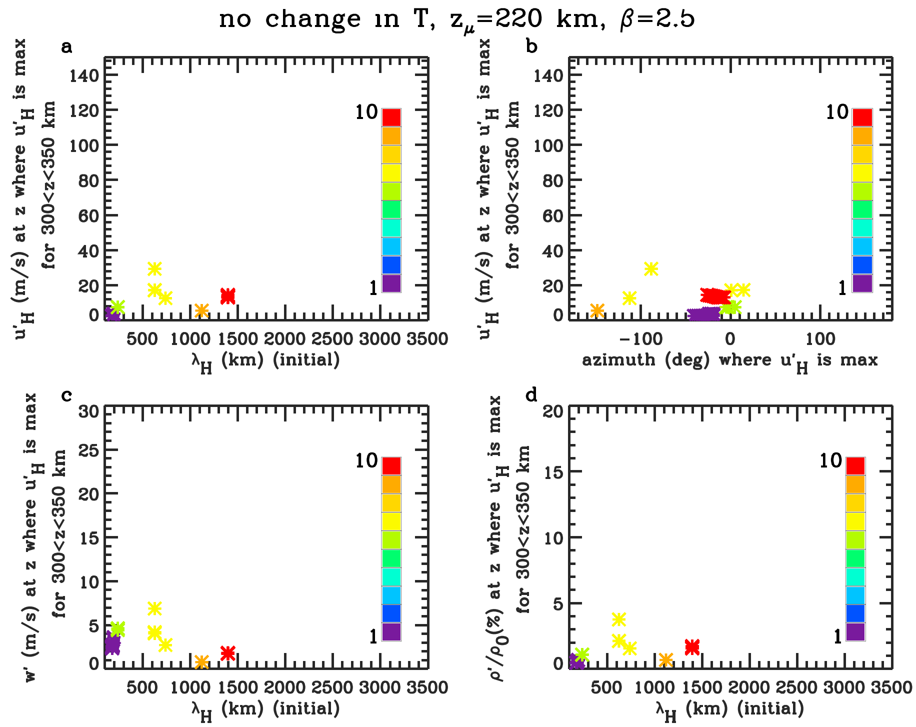

Figure 13. Same as in Figure 12 but for $\beta = 2.5$.

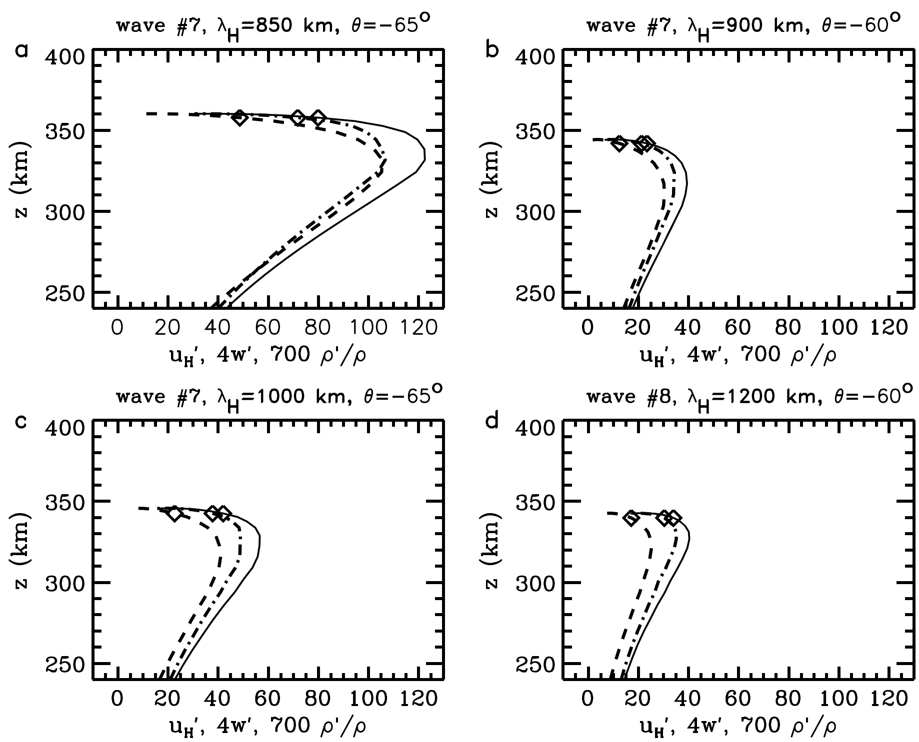

Figure 14. Amplitudes of u'_H (solid, in m/s), $4w'$ (dash, in m/s), and $700\rho'/\bar{\rho}$ (dash-dotted) as a function of altitude. The background atmosphere is the combined ECMWF/TIME-GCM model with $z_\mu = 220$ km and $\beta = 2$. (a) GW # 7 with initial values (at $z = z_i$) of $\lambda_H = 850$ km, $\lambda_z = -400$ km, $\theta = -65°$, and $\tau_{Ir} = 30.5$ min. (b) GW # 7 with initial values $\lambda_H = 900$ km, $\lambda_z = -350$ km, $\theta = -60°$, and $\tau_{Ir} = 33.4$ min. (c) GW # 7 with initial values $\lambda_H = 1000$ km, $\lambda_z = -400$ km, $\theta = -65°$, and $\tau_{Ir} = 35$ min. (d) GW # 8 with initial values $\lambda_H = 1200$ km, $\lambda_z = -500$ km, $\theta = -60°$, and $\tau_{Ir} = 39$ min. The diamonds show where the residue equals 1.

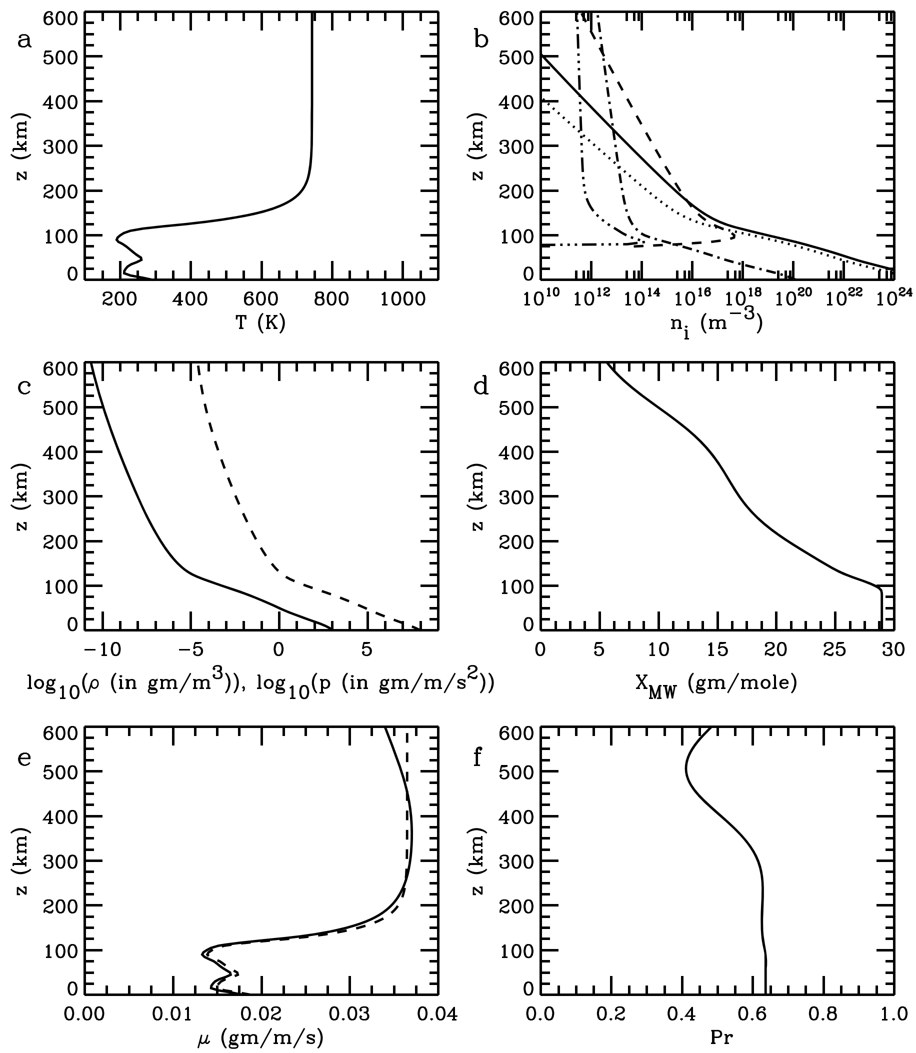

Figure 15. (a) MSIS temperature profile on 30 October 2007 at 0415 UT. (b) MSIS number densities of the major species: n_{N_2} (solid), n_{O_2} (dot), n_O (dash), n_{He} (dash-dotted), and n_H (dash-dot-dot-dot). (c) $\log_{10}(\bar{\rho})$ (solid line) and $\log_{10}(\bar{p})$ (dashed line). Here $\bar{\rho}$ is in gm/m^3, and $\bar{p}$ is in gm/m/s^2. (d) Mean molecular mass X_{MW} in gm/mol. (e) μ from equation (55) using MSIS number densities (solid line), and μ from equation (46) (dashed line). (f) Prandtl number, Pr, calculated from equation (58).

6. Viscosity and Thermal Conductivity That Include All Major Species

The expression used here for μ (i.e., equation (46)) only includes atomic oxygen, which is the most important species throughout most of the thermosphere. Thus, this expression neglects the viscosities of O_2, N_2, He, and H. Because the molecular viscosities of O_2, N_2, He are similar to that of O [*Banks and Kockarts*, 1973b, equations (14.34)–(14.37)], it is reasonable to neglect these species throughout most of the thermosphere. Hydrogen's molecular viscosity, however, is ∼3 times smaller. This causes a noticeable decrease in μ for $z > 500$ km [*Banks and Kockarts*, 1973b, Figure 14.1]. Additionally, although the thermal conductivity is relatively constant for $200 < z < 400$ km, it increases substantially at $z > 450$ km because of He and H [*Banks and Kockarts*, 1973b, Figure 14.4]. This increase corresponds to a decrease in the Prandtl number at $z > 450$ km.

The departure of μ away from equation (46) is only significant for $z > 450$ km, which is well above the altitude where u'_H peaks in Figure 1a. Regardless, we now investigate whether including all major species in our formulas for μ and Pr changes our basic results and conclusions from section 5.

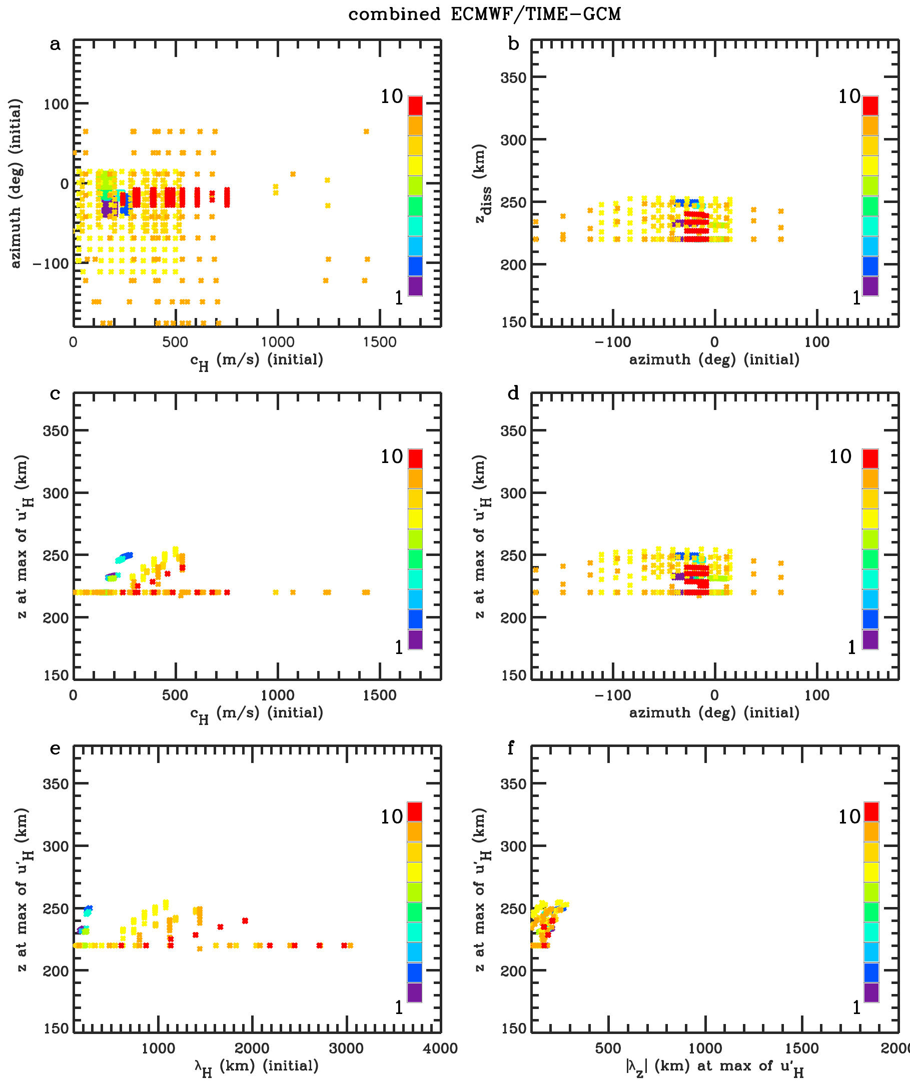

Figure 16. Same as in Figure 3 but using the combined ECMWF/TIME-GCM model for the background atmosphere, setting $Pr = 0.62$ and using μ from equation (55).

The molecular viscosity can be written as follows:

$$\mu = \frac{\left(4.03n_{O_2} + 3.43n_{N_2} + 3.90n_{O} + 3.84n_{He} + 1.22n_{H}\right) \times 10^{-4}\, \bar{T}^{0.69}}{n_{O_2} + n_{N_2} + n_{O} + n_{He} + n_{H}} \text{ gm m}^{-1}\,\text{s}^{-1}, \tag{55}$$

where n_i is the number of molecules per m^3 of the ith species [*Banks and Kockarts*, 1973b, equations (14.34)–(14.40)]. The thermal conductivity (expressed as "λ" in *Banks and Kockarts* [1973b] but which we relabel here as "ζ") is

$$\zeta = \frac{\left(56(n_{O_2} + n_{N_2}) + 75.9n_{O} + 299n_{He} + 379n_{H}\right) \times 10^{-2}\, \bar{T}^{0.69}}{n_{O_2} + n_{N_2} + n_{O} + n_{He} + n_{H}} \text{ gm m s}^{-3}\text{K}^{-1} \tag{56}$$

(equations (14.43)–(14.45) and (14.48) and the discussion following equation (14.51) in *Banks and Kockarts* [1973b]). (Note that equations (55) and (56)) are identical to equations (A3) and (A4) in *Yu et al.* [2015], except that *Yu et al.* [2015] neglected He and H.) The corresponding energy equation is written as $DT/Dt =$ "*stuff*" $+\zeta/(C_v\rho)\nabla^2 T$ [*Banks and Kockarts*, 1973b, equations (14.21) and (14.22)], where $D/Dt = (\partial/\partial t + \mathbf{v}.\nabla)$, $\mathbf{v}$ is the

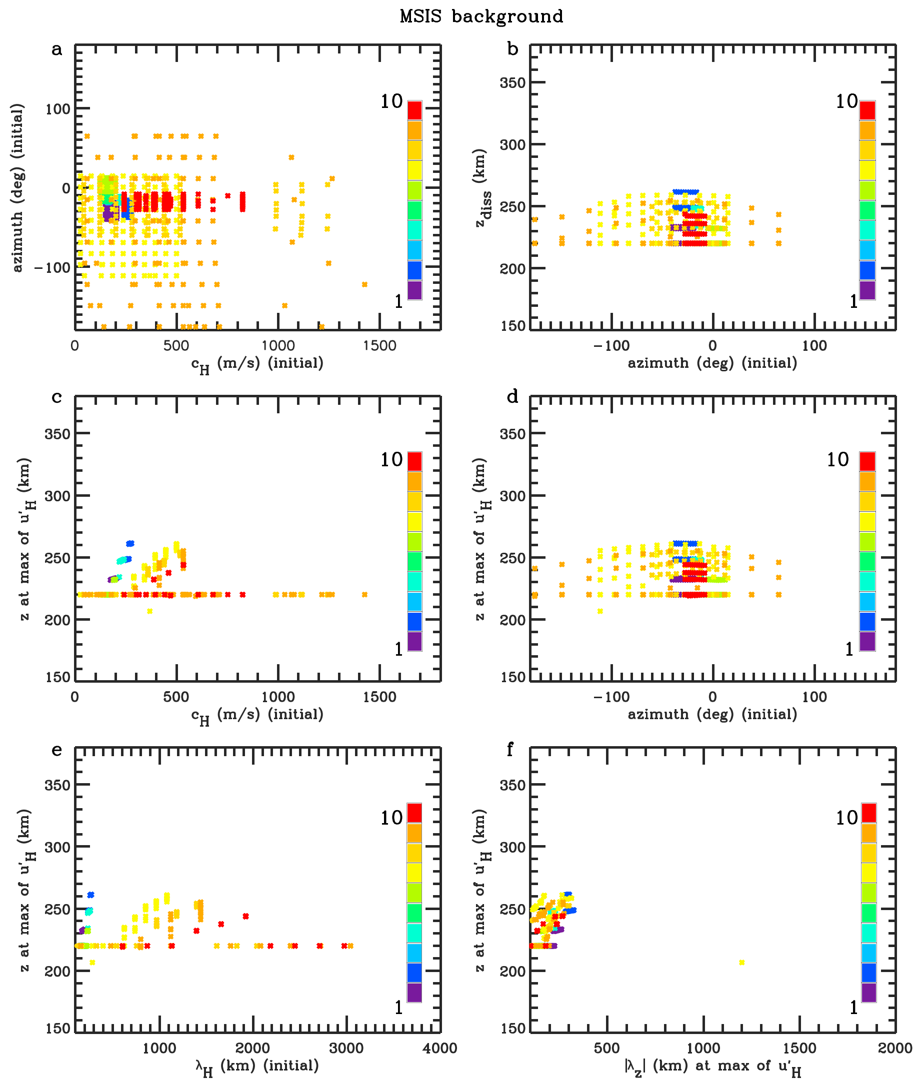

Figure 17. Same as in Figure 3 but using the MSIS model shown in Figure 15 for the background atmosphere, setting $Pr = 0.62$ and using μ from equation (55).

velocity, and *stuff* represents other terms in the energy equation. The energy equation can also be written as $DT/Dt = stuff + (\gamma\mu)/(Pr\rho)\nabla^2 T$ [e.g., *Vadas and Nicolls*, 2012]. Setting the prefactors for the thermal conductivity terms equal, we obtain

$$\frac{\gamma\mu}{Pr\rho} = \frac{\zeta}{C_v\rho}. \tag{57}$$

Rearranging and using $C_v = R/(\gamma - 1)$ and $C_p = \gamma R/(\gamma - 1)$, where C_p is the mean specific heat at constant pressure, the Prandtl number can be expressed as

$$Pr = \frac{\gamma R}{(\gamma - 1)}\frac{\mu}{\zeta} = C_p\frac{\mu}{\zeta}. \tag{58}$$

Figure 15a shows the MSIS temperature $\bar{T}$ on 30 October 2007 at 0415 UT. The exospheric temperature is $\bar{T} = 743$ K. Figure 15b shows the corresponding concentrations of the major species up to $z = 600$ km. For $z < 100$ km, N_2 and O_2 are the major constituents, as expected. For $150 < z < 500$ km, O is the major constituent. For $z = 500$–600 km, He is the major constituent. Figure 15c shows $\log_{10}\bar{\rho}$ and $\log_{10}\bar{p}$. These quantities decrease by ~11–12 orders of magnitude between the surface and $z \sim 400$ km. Figure 15d shows X_{MW}. Atomic oxygen dominates for $200 < z < 400$ km, where $X_{MW} \sim 16$ gm/mol. Above that altitude, He becomes increasingly important (with $X_{MW} \rightarrow 4$ gm/mol). Figure 15e shows μ calculated from equation (55). We see that μ

follows $\bar{T}$ fairly closely for $z < 450$ km because of the $\bar{T}^{0.69}$ dependence in that formula. For $z > 450$ km, however, μ decreases significantly with altitude. We also overplot μ from equation (46). This simple expression agrees quite well with equation (55) for $z < 450$ km. This is because the molecular viscosity formulas are similar for all of the major species except H, which only begins to be important for $z > 500$ km. Figure 15f shows the Prandtl number calculated from equation (58). Pr is relatively constant for $z < 300$ km with a value of $Pr = 0.62$, decreases for $300 < z < 500$ km, and increases for $z > 500$ km. We expect that the decrease of Pr for $300 < z < 400$ km will result in increased GW damping (and therefore somewhat smaller z_{diss}) for the TIDDBIT GWs that are able to propagate to $z \sim 325$ km, since $\mu \simeq$ constant for $250 < z < 400$ km from Figure 15e.

We ray trace all TIDDBIT GWs as before using the combined ECMWF/TIME-GCM model as the background atmosphere, but with $Pr = 0.62$ and replacing equation (46) with equation (55). The results are shown in Figure 16. These results are quite similar to Figure 3, except that no GW has its u'_H maximum above $z \simeq 260$ km. This is lower than in Figure 3 because Pr is somewhat smaller here.

We now ray trace all TIDDBIT GWs using the MSIS model shown in Figures 15a-15d as the background atmosphere, set $Pr = 0.62$, and replace equation (46) with equation (55). Figure 17 shows the results. We see that z_{diss} and the altitudes where u'_H are maxima are again quite similar to Figure 3. Additionally, none of the GWs have their u'_H maximum above $z \sim 270$ km. Therefore, including all of the major species in the expressions for the molecular viscosity and thermal conductivity does not substantially change the results and conclusions of this paper.

7. Conclusions

In this paper, we determined the parameters (including the Doppler wave amplitudes) for the 10 TIDDBIT TIDs observed on the evening of 30 October 2007 at Wallops Island during a coordinated rocket experiment [*Earle et al.*, 2010]. These TIDs were observed at $z_{\text{obs}} \simeq 283$ km and were previously shown to be secondary GWs excited by deep convection in tropical storm Noel using reverse ray tracing (VC10). Because *Earle et al.* [2010] found a neutral horizontal wind peak, u'_H, at $z \sim 325$ km which was in the direction of propagation of the GWs, we wished to determine if several of these TIDDBIT GWs could have contributed to this wind peak. Therefore, we forward ray traced these TIDDBIT GWs here in order to determine the neutral wind and density perturbations created by these GWs at higher altitudes. For this purpose, we used the measured Doppler wave amplitudes of the TIDs to determine the GW amplitudes at the TIDDBIT observation altitude. We then used the forward ray trace results and GW dissipative theory to determine the GW amplitudes at all altitudes. Note that this forward ray trace method does not take into account the origin of these TIDDBIT GWs—it only utilizes the fact that the GWs were observed at z_{obs}.

We constructed a background atmosphere for ray tracing using combined ECMWF and TIME-GCM data. We included the errors in λ_H and θ via ray tracing 100 GWs for each TIDDBIT GW. Additionally, we launched the GWs from a lower-than-observed altitude (i.e., $z_i = 220$ km) in order to determine how high each GW could propagate. We found that all but one of the TIDDBIT GWs would have dissipated more than H below z_{obs} and therefore could not have been observed at $z = z_{\text{obs}}$. Additionally, none of the GWs could have caused the u'_H peak at $z \sim 325$ km measured by the rocket. These results constituted a serious discrepancy between GW dissipative theory and observations.

In order to better understand the nature of the difficulty, we investigated several possible reasons for this discrepancy. This included the possibility that (1) the background temperature $\bar{T}$ used for ray tracing was smaller than the actual $\bar{T}$ that night and (2) that the molecular viscosity μ did not have the correct functional form at altitudes in the middle to upper thermosphere where this routinely used formula was essentially untested. Via comparison with the MSIS empirical model and Millstone Hill ion temperatures, we found that the TIME-GCM $\bar{T}$ may have been 30–90 K lower than the actual $\bar{T}$ that evening. We therefore performed sensitivity experiments in order to see how much $\bar{T}$ needed to be increased by in order to yield a peak in u'_H at $z \sim 325$ km. We found that we needed to increase $\bar{T}$ by 225 K, which was much larger than the possible discrepancy between the TIME-GCM $\bar{T}$ and the actual $\bar{T}$ that evening. Therefore, we concluded that the effect from a smaller-than-realistic $\bar{T}$ could not have accounted for the low propagation altitudes of the TIDDBIT GWs.

We investigated the routinely used formula for μ [*Dalgarno and Smith*, 1962], which accounts for the molecular viscosity of atomic oxygen, and found that it was derived under the assumption that the average separation distance between molecules was 10 to tens of atomic units. We computed the molecular separation distance in the thermosphere and found that it is hundreds of thousands of atomic units at $z \sim 250$ km. Therefore, we reasoned that the *Dalgarno and Smith* [1962] formula for μ (for which $\mu \sim$ constant at $z > 220$ km) might not be applicable in the middle to upper thermosphere. Because an ideal gas has $\bar{p} = R\bar{\rho}\bar{T}$, $\bar{T}$ can be large even though $\bar{\rho}$ and $\bar{p}$ are extremely small. (In fact, $\bar{T}$ is large in the thermosphere because of heat influx from solar radiation, even though $\bar{p}$ and $\bar{\rho}$ are extremely small there.) In the limit that $\bar{\rho}$ and $\bar{p}$ go to zero for a fixed $\bar{T}$, it seems self-evident that μ must $\rightarrow 0$ because the distance between molecules $\rightarrow \infty$, thereby implying no collisions and therefore no viscosity. Therefore, we reasoned that μ must decrease somewhere in the middle to upper thermosphere.

We hypothesized that $\mu \propto \bar{\rho}^{\beta/3}$ for $z \geq z_\mu$ in the middle to upper thermosphere. Because the formula for μ agreed well with observational data for $z < 225$ km in previous studies [*Vadas*, 2007], we therefore only decreased μ above this approximate altitude. We then ray traced the TIDDBIT GWs through the thermosphere using $z_\mu = 220$, 250, and 270 km with $\beta = 1.5$, 2, 2.5, and 3. We found that $z_\mu = 220$ km and $\beta = 2$ resulted in u'_H peaking at $z \sim 325$ km for several of the TIDDBIT GWs, thereby implying that one or several of these GWs may have caused this wind peak observed by the rocket. Additionally, all of the TIDDBIT GWs could have been observed at $z = z_{\text{obs}}$ for $z_\mu = 220$ km and $\beta = 2$.

Finally, we investigated the possibility that μ might be too large because the *Dalgarno and Smith* [1962] formula for μ only takes into account atomic oxygen. We therefore included all molecular species in the thermosphere using the formula for μ from *Banks and Kockarts* [1973b]. Here we used the number densities calculated from MSIS. We found that the profile for μ was essentially the same up to $z \sim 500$ km, although the Prandtl number *Pr* decreased somewhat at $300 < z < 400$ km. We ray traced the TIDDIBT GWs with this *Banks and Kockarts* [1973b] formula and a slightly smaller *Pr* with and without the the MSIS $\bar{T}$ and $\bar{\rho}$ and found that the results were essentially unchanged from the original results. Therefore, we concluded that including all of the molecular species could not explain the serious discrepancy between GW dissipative theory and the TIDDBIT/rocket data.

In conclusion, we have found that the molecular viscosity, μ, is too large in the middle to upper thermosphere using the standard formulas for μ from *Dalgarno and Smith* [1962] or *Banks and Kockarts* [1973b]. We have found that using these formulas leads to a serious discrepancy between GW theory and the TIDDIT/rocket data. (Note that this conclusion does not rely on the origin of the TIDDBIT GWs (i.e., thermospheric body forces).) We found that implementing an empirical formula with μ decreasing via $\mu \propto \bar{\rho}^q$ with $q \sim 0.67$ (i.e., $\mu \propto 1/d^2$, where d is the average separation distance between molecules) for $z \geq 220$ km yields results that agree much better with the observations. This implies that the kinematic viscosity, $\nu = \mu/\bar{\rho}$, increases less rapidly with altitude for $z \geq 220$ km: $\nu \propto 1/\bar{\rho}^{0.33}$. For $z > 200$ km, $\bar{\rho} \propto \exp(-z/H)$, where H is the neutral density scale height. Therefore, our result implies that $\nu \propto \exp(z/3H)$ for $z \geq 220$ km. Because ν increases less rapidly in the middle to upper thermosphere as compared to $\mu =$ constant, it is possible that our result implies that the tidal amplitudes might be different in the middle to upper thermosphere; however, because the tides do not change appreciably for $z > 200$ km when $\mu =$ constant, and the decrease in μ only occurs for $z \geq 220$ km, we do not expect the tidal amplitudes to change significantly. Future works will investigate the theoretical understanding and implications for GWs and tides caused by a decreasing molecular viscosity in the middle to upper thermosphere.

Acknowledgments
S.L.V. was supported by NASA contract NNH12CE58C and NSF grant AGS-1552315. G.C. was supported by NASA grant NNH12CE58C and LCAS grant NG04WC22G. We would like to thank Tim Duly for technical help with the MSIS and Millstone Hill data displayed in this paper. We acknowledge and thank ECMWF/ERA-Interim for the use of their lower atmospheric meteorological data. The data shown in this paper may be available for collaborative research pending an e-mail request to the authors.

References

Banks, P. M., and G. Kockarts (1973a), *Aeronomy Part A*, 430 pp., Academic Press, New York.

Banks, P. M., and G. Kockarts (1973b), *Aeronomy Part B*, 355 pp., Academic Press, New York.

Becker, E. (2017), Mean-flow effects of thermal tides in the mesosphere and lower thermosphere, *J. Atmos. Sci.*, doi:10.1175/JAS-D-16-0194.1.

Conde, M. G., and M. J. Nicolls (2010), Thermospheric temperatures above Poker Flat, Alaska, during the stratospheric warming event of January and February 2009, *J. Geophys. Res.*, *115*, D00N05, doi:10.1029/2010JD014280.

Crowley, G., and F. S. Rodrigues (2012), Characteristics of traveling ionospheric disturbances observed by the TIDDBIT sounder, *Radio Sci.*, *47*, RS0L22, doi:10.1029/2011RS004959.

Crowley, G., A. Reynolds, J. P. Thayer, J. Lei, L. J. Paxton, A. B. Christensen, Y. Zhang, R. R. Meier, and D. J. Strickland (2008), Periodic modulations in thermospheric composition by solar wind high speed streams, *Geophys. Res. Lett.*, *35*, L21106, doi:10.1029/2008GL035745.

Crowley, G., D. J. Knipp, K. A. Drake, J. Lei, E. Sutton, and H. Lühr (2010), Thermospheric density enhancements in the dayside cusp region during strong B_Y conditions, *Geophys. Res. Lett.*, *37*, L07110, doi:10.1029/2009GL042143.

Dalgarno, A., and F. J. Smith (1962), The thermal conductivity and viscosity of atomic oxygen, *Planet. Space Sci.*, *9*, 1–2.

DelGenio, A. D., and G. Schubert (1979), Gravity wave propagation in a diffusively separated atmosphere with height-dependent collision frequencies, *J. Geophys. Res.*, *84*, 4371–4378.

Earle, G. D., et al. (2010), A comprehensive rocket and radar study of midlatitude spread F, *J. Geophys. Res.*, *115*, A12339, doi:10.1029/2010JA015503.

Einaudi, F., and C. O. Hines (1970), WKB approximation in application to acoustic-gravity waves, *Can. J. Phys.*, *48*, 1458–1471.

Fritts, D. C., and M. J. Alexander (2003), Gravity wave dynamics and effects in the middle atmosphere, *Rev. Geophys.*, *41*, 1003, doi:10.1029/2001RG000106.

Fritts, D. C., and S. Vadas (2008), Gravity wave penetration into the thermosphere: Sensitivity to solar cycle variations and mean winds, *Ann. Geophys.*, *26*, 3841–3861, doi:10.5194/angeo-26-3841-2008.

Godin, O. A. (2015), Wentzel-Kramers-Brillouin approximation for atmospheric waves, *J. Fluid Mech.*, *777*, 260–290, doi:10.1017/jfm.2015.367.

Gossard, E. E., and W. H. Hooke (1975), *Waves in the Atmosphere*, 456 pp., Elsevier Scientific Publ., Amsterdam.

Heale, C. J., J. B. Snively, M. P. Hickey, and C. J. Ali (2014), Thermospheric dissipation of upward propagating gravity wave packets, *J. Geophys. Res. Space Physics*, *119*, 3857–3872, doi:10.1002/2013JA019387.

Hickey, M. P., and K. D. Cole (1988), A numerical model for gravity wave dissipation in the thermosphere, *J. Atmos. Terr. Phys.*, *50*, 689–697.

Hines, C. O. (1960), Internal atmospheric gravity waves at ionospheric heights, *Can. J. Phys.*, *38*, 1441–1481.

Hocke, K., and K. Schlegel (1996), A review of atmospheric gravity waves and traveling ionospheric disturbances, *Ann. Geophys.*, *14*, 917–940.

Kirchengast, G., K. Hocke, and K. Schlegel (1996), The gravity wave-TID relationship: Insight via theoretical model-EISCAT data comparison, *J. Atmos. Terr. Phys.*, *58*, 233–243.

Klostermeyer, J. (1972), Numerical calculation of gravity wave propagation in a realistic thermosphere, *J. Atmos. Terr. Phys.*, *34*, 765–774.

Kundu, P. (1990), *Fluid Mechanics*, 638 pp., Academic Press, San Diego, Calif.

Liu, X., J. Xu, J. Yue, and S. L. Vadas (2013), Numerical modeling study of the momentum deposition of small amplitude gravity waves in the thermosphere, *Ann. Geophys.*, *31*, 1–14.

Ma, J. Z. G. (2016), Atmospheric layers in response to the propagation of gravity waves under nonisothermal, wind-shear, and dissipative conditions, *J. Mar. Sci. Eng.*, *4*, 25.

Marks, C. J., and S. D. Eckermann (1995), A three-dimensional nonhydrostatic ray-tracing model for gravity waves: Formulation and preliminary results for the middle atmosphere, *J. Atmos. Sci.*, *52*, 1959–1984.

Nicolls, M. J., S. L. Vadas, J. W. Meriwether, M. G. Conde, and D. Hampton (2012), The phases and amplitudes of gravity waves propagating and dissipating in the thermosphere: Application to measurements over Alaska, *J. Geophys. Res.*, *117*, A05323, doi:10.1029/2012JA017542.

Nicolls, M. J., S. L. Vadas, N. Aponte, and M. P. Sulzer (2014), Horizontal wave parameters of daytime thermospheric gravity waves and E-region neutral winds over Puerto Rico, *J. Geophys. Res. Space Physics*, *119*, 575–600, doi:10.1002/2013JA018988.

Picone, J. M., A. E. Hedin, D. P. Drob, and A. C. Aikin (2002), NRLMSISE-00 empirical model of the atmosphere: Statistical comparisons and scientific issues, *J. Geophys. Res.*, *107*(A12), 1468, doi:10.1029/2002JA009430.

Pitteway, M. L. V., and C. O. Hines (1963), The viscous damping of atmospheric gravity waves, *Can. J. Phys.*, *41*, 1935–1948.

Roble, R. G., and E. C. Ridley (1994), A thermosphere-ionosphere-mesosphere-electrodynamics general circulation model (TIME-GCM): Equinox solar cycle minimum simulations (30–500 km), *Geophys. Res. Lett.*, *21*, 417–420.

Vadas, S. L. (2007), Horizontal and vertical propagation and dissipation of gravity waves in the thermosphere from lower atmospheric and thermospheric sources, *J. Geophys. Res.*, *112*, A06305, doi:10.1029/2006JA011845.

Vadas, S. L. (2013), Compressible F-plane solutions to body forces, heatings, and coolings, and application to the primary and secondary gravity waves generated by a deep convective plume, *J. Geophys. Res. Space Physics*, *118*, 2377–2397, doi:10.1002/jgra.50163.

Vadas, S. L., and G. Crowley (2010), Sources of the traveling ionospheric disturbances observed by the ionospheric TIDDBIT sounder near Wallops Island on October 30, 2007, *J. Geophys. Res.*, *115*, A07324, doi:10.1029/2009JA015053.

Vadas, S. L., and D. C. Fritts (2005), Thermospheric responses to gravity waves: Influences of increasing viscosity and thermal diffusivity, *J. Geophys. Res.*, *110*, D15103, doi:10.1029/2004JD005574.

Vadas, S. L., and D. C. Fritts (2009), Reconstruction of the gravity wave field from convective plumes via ray tracing, *Ann. Geophys.*, *27*, 147–177.

Vadas, S. L., and H.-L. Liu (2009), The generation of large-scale gravity waves and neutral winds in the thermosphere from the dissipation of convectively-generated gravity waves, *J. Geophys. Res.*, *114*, A10310, doi:10.1029/2009JA014108.

Vadas, S. L., and H.-L. Liu (2013), Numerical modeling of the large-scale neutral and plasma responses to the body forces created by the dissipation of gravity waves from 6 h of deep convection in Brazil, *J. Geophys. Res. Space Physics*, *118*, 2593–2617, doi:10.1002/jgra.50249.

Vadas, S. L., and M. J. Nicolls (2009), Temporal evolution of neutral, thermospheric winds and plasma response using PFISR measurements of gravity waves, *J. Atmos. Sol. Terr. Phys.*, *71*, 740–770.

Vadas, S. L., and M. J. Nicolls (2012), The phases and amplitudes of gravity waves propagating and dissipating in the thermosphere: Theory, *J. Geophys. Res.*, *117*, A05322, doi:10.1029/2011JA017426.

Vadas, S. L., J. Yue, C.-Y. She, P. A. Stamus, and A. Liu (2009), A model study of the effects of winds on concentric rings of gravity waves from a convective plume near Fort Collins on 11 May 2004, *J. Geophys. Res.*, *114*, D06103, doi:10.1029/2008JD010753.

Volland, H. (1969), The upper atmosphere as a multiply refractive medium for neutral air motions, *J. Atmos. Terr. Phys.*, *31*, 491–514.

Walterscheid, R. L., and M. P. Hickey (2011), Group velocity and energy flux in the thermosphere: Limits on the validity of group velocity in a viscous atmosphere, *J. Geophys. Res.*, *116*, D12101, doi:10.1029/2010JD014987.

Yanowitch, M. (1967), Effect of viscosity on gravity waves and the upper boundary condition, *J. Fluid Mech.*, *29*, 209–231.

Yeh, K. C., and C. H. Liu (1974), Acoustic gravity waves in the upper atmosphere, *Rev. Geophys.*, *12*(2), 193–216, doi:10.1029/RG012i002p00193.

Yeh, K. C., C. H. Liu, and M. Y. Youakim (1975), Attenuation of internal gravity waves in model atmospheres, *Ann. Geophys.*, *31*, 321–328.

Yiğit, E., A. S. Medvedev, A. D. Aylward, P. Hartogh, and M. J. Harris (2009), Modeling the effects of gravity wave momentum deposition on the general circulation above the turbopause, *J. Geophys. Res.*, *114*, D07101, doi:10.1029/2008JD011132.

Yu, Y., Z. Yan, and M. P. Hickey (2015), Lower thermospheric response to atmospheric gravity waves induced by the 2011 Tohoku tsunami, *J. Geophys. Res. Space Physics*, *120*, 5062–5075, doi:10.1002/2015JA020986.

Yu, Y., W. Wang, and M. P. Hickey (2017), Ionospheric signatures of gravity waves produced by the 2004 Sumatra and 2011 Tohoku tsunamis: A modeling study, *J. Geophys. Res. Space Physics*, *122*, 1146–1162, doi:10.1002/2016JA023116.